

Travail de fin d'études et stage[BR]- Travail de fin d'études : Analytical model of an electromagnetic linear actuator and its design optimisation[BR]- Stage d'insertion professionnelle

Auteur : Ruelle, Bastien

Promoteur(s) : Duysinx, Pierre

Faculté : Faculté des Sciences appliquées

Diplôme : Master en ingénieur civil mécanicien, à finalité spécialisée en technologies durables en automobile

Année académique : 2021-2022

URI/URL : <http://hdl.handle.net/2268.2/15983>

Avertissement à l'attention des usagers :

Tous les documents placés en accès ouvert sur le site le site MatheO sont protégés par le droit d'auteur. Conformément aux principes énoncés par la "Budapest Open Access Initiative"(BOAI, 2002), l'utilisateur du site peut lire, télécharger, copier, transmettre, imprimer, chercher ou faire un lien vers le texte intégral de ces documents, les disséquer pour les indexer, s'en servir de données pour un logiciel, ou s'en servir à toute autre fin légale (ou prévue par la réglementation relative au droit d'auteur). Toute utilisation du document à des fins commerciales est strictement interdite.

Par ailleurs, l'utilisateur s'engage à respecter les droits moraux de l'auteur, principalement le droit à l'intégrité de l'oeuvre et le droit de paternité et ce dans toute utilisation que l'utilisateur entreprend. Ainsi, à titre d'exemple, lorsqu'il reproduira un document par extrait ou dans son intégralité, l'utilisateur citera de manière complète les sources telles que mentionnées ci-dessus. Toute utilisation non explicitement autorisée ci-avant (telle que par exemple, la modification du document ou son résumé) nécessite l'autorisation préalable et expresse des auteurs ou de leurs ayants droit.



Analytical model of an electromagnetic linear actuator and its design optimisation

*Master thesis conducted for obtaining the Master's degree of Science in
Mechanical Engineering major in Sustainable Automotive*

Bastien Ruelle - 20172395

SUPERVISOR: DUYSINX Pierre

UNIVERSITY OF LIÈGE
FACULTY OF APPLIED SCIENCES
ACADEMIC YEAR 2021 - 2022

Optimisation on the analytical model of an electromagnetic linear actuator

Bastien Ruelle

Faculty: Applied Sciences at the University of Liège

Section: Mechanical Engineering

Supervisor: Pierre Duysinx

Academic year 2021-2022

Abstract

This Master's Thesis aims to produce a tubular permanent magnet actuator (TPMA) design capable of replacing the hydraulic dampers present in active train suspensions. This design needs to be optimised to provide the best possible performance.

In the first part of this thesis, a state of the art of the available TPMA topologies is presented as well as their operating principle.

In the second part the analytical model of each topology is developed in order to obtain the behaviour of the magnetic flux within each actuator. This model contains the solution of the Laplace and Poisson equations from Maxwell's equations. The specific boundary conditions for each of the topologies are exposed in order to obtain the specific solutions. Then the results are compared in order to keep the best topology for the rest of the thesis.

The third part is devoted to the modelling of the thrust produced by the actuator. The thrust produced by the actuator is dependent on the type of current injected. Thus three types of current are compared: single-phase, two-phase and three-phase.

The fourth part concerns the optimisation of the actuator design. In a first step, the optimisation is done by the particle swarm optimisation (PSO) method. This first optimisation has only one objective, to maximise the thrust produced by the actuator. The dimensions to be optimised are the radii of the actuator and the pole pitch of the magnets. In a second step, a new objective, that of minimising the force variation, is added to the optimisation. This multi-objective optimisation problem is solved using a method derived from PSO: vector evaluated particle swarm optimisation. Finally, the different designs obtained by the two optimisations are compared.

The last part is devoted to the presentation of some improvements that could be made to the analytical model of the actuator to make it even more accurate.

Optimisation sur le modèle analytique d'un actionneur linéaire électromagnétique

Bastien Ruelle

Faculté: Sciences Appliquées à l'Université de Liège

Section: Ingénieur Mécanicien

Promoteur: Pierre Duysinx

Année Académique 2021-2022

Résumé

Cette thèse de Master vise à produire un design d'actionneur tubulaire à aimants permanents capable de remplacer les amortisseurs hydrauliques présents dans les suspensions actives de train. Ce design se doit d'être optimisé afin de fournir les meilleures performances possibles.

Dans la première partie de cette thèse, un état de l'art des topologies d'actionneur tubulaire à aimants permanents disponibles ainsi que leur principe de fonctionnement sont présentés.

Dans la seconde partie le modèle analytique de chacune des topologies est développé afin d'obtenir le comportement du flux magnétique au sein de chaque actionneur. Ce modèle contient la résolution des équations de Laplace et de Poisson provenant des équations de Maxwell. Les conditions limites spécifiques à chacune des topologies sont exposées afin d'obtenir les solutions spécifiques. Ensuite les résultats sont comparés afin de conserver la meilleure topologie pour la suite de la thèse.

La troisième partie est consacrée à la modélisation de la poussée produite par l'actionneur. La poussée produite par l'actionneur est dépendante du type de courant injecté. Ainsi trois types de courant sont comparés: monophasé, biphasé et triphasé.

La quatrième partie concerne l'optimisation du design de l'actionneur. Dans un premier temps, l'optimisation est faite par la méthode de la "particle swarm optimisation (PSO)". Cette première optimisation a un seul objectif, celui de maximiser la poussée produite par l'actionneur. Les dimensions à optimiser sont les rayons de l'actionneur ainsi que la largeur du pas du pôle des aimants. Dans un second temps, un nouvel objectif, celui de minimiser la fluctuation de la poussée, se rajoute à l'optimisation. Ce problème d'optimisation à plusieurs objectifs est résolu en utilisant une méthode dérivée de la PSO: la "vector evaluated particle swarm optimisation". Finalement les différents designs obtenus par les deux optimisations sont comparés.

La dernière partie est consacrée à la présentation de certaines améliorations qui pourraient être apportées au modèle analytique de l'actionneur afin qu'il soit encore plus précis.

Acknowledgements

I would like to thank Prof. P. Duysinx, my thesis supervisor, for giving me the opportunity to do this thesis. I feel grateful for his wise advice and especially for his encouragement that allowed me to progress in this project.

Liège, August 22th, 2022

Bastien Ruelle

Contents

1	Introduction	1
1.1	Context of the project	1
1.2	Description of the technology	1
1.3	The project	3
1.3.1	Objectives of the project	3
1.3.2	Structure of the thesis	3
	Chapter 1:	3
	Chapter 2:	3
	Chapter 3:	4
	Chapter 4:	4
	Chapter 5:	4
	Chapter 6:	4
1.3.3	State of art	4
1.3.4	Topologies studied in the thesis	6
2	Analytical Model of Magnetic field	9
2.1	Assumptions	9
2.2	Governing equations of flux field	10
2.2.1	Laplace's equation for the air gap region	10
2.2.2	Poisson's equation for the permanent magnet region	11
2.3	Solution to flux density distribution	11
2.3.1	Solution to Laplace's equation	11
2.3.2	Solution to Poisson's equation	13
	2.3.2.1 Halbach array topology	13
	2.3.2.2 Radially magnetised PM array topology	15
	2.3.2.3 Axially magnetised PM array topology	16
2.4	Boundary conditions	18
2.4.1	Dual Halbach array topology	18
2.4.2	Radially magnetised PM array topology	20
2.4.3	Axially magnetised PM array topology	21
2.5	Representation of results	22
2.5.1	Note on calculations involving Bessel functions	22
2.5.2	Dual Halbach array topology	23
	2.5.2.1 Validation of boundary conditions	24
	2.5.2.2 Magnetic flux density in the PM region	24
	2.5.2.3 Magnetic flux density in the air gap region	25
2.5.3	Radially magnetised PM array topology	26

2.5.3.1	Validation of boundary conditions	26
2.5.3.2	Magnetic flux density in the magnetic region	26
2.5.3.3	Magnetic flux density in the air gap region	28
2.5.4	Axially magnetised PM array topology	28
2.5.4.1	Validation of boundary conditions	29
2.5.4.2	Magnetic flux density in the magnetic region	29
2.5.4.3	Magnetic flux density in the air gap region	30
3	Modeling of Force Output	31
3.1	Assumptions	32
3.2	Thrust for Single-Phase Winding Pattern	32
3.3	Thrust for Double-Phase Winding Pattern	34
3.4	Thrust for Three-Phase Winding Pattern	37
3.5	Conclusion	40
4	Optimisation of the design	41
4.1	SOO problem	41
4.1.1	Definition and Mathematical formulation of the problem	41
4.1.2	PSO Resolution	42
4.2	MOO problem	47
4.2.1	Definition and Mathematical formulation of the problem	47
4.2.2	VEPSO Resolution	48
5	Improvement and further research	52
5.1	Finite permeability back iron parts	52
5.2	Finite length TPMA	53
5.3	Armature field reaction	54
5.4	Incorporation of TPMA into the suspension system	55
6	Conclusion	58

List of Figures

1.1	Evolution of rotary motor to linear machine [2]	2
1.2	Complete structure of a TPMA [4]	3
1.3	Most commonly used TPMA topologies [5]	5
1.4	Slotless and Slotted armature topologies [4]	5
1.5	Cogging force produced by the offset between the mover teeth and the PMs [6]	6
1.6	Scheme of radially magnetized PM topology [5]	6
1.7	Scheme of axially magnetized PM topology [5]	7
1.8	Structure of dual Halbach array TPMA [8]	7
1.9	Polarization pattern arrays of TPMA [9]	7
1.10	One-sided flux [11]	8
1.11	Scheme of Halbach magnetized PM topology	8
2.1	Halbach array : components of magnetization vector [15]	13
2.2	Radially magnetised PMs : components of magnetization vector [15]	15
2.3	Axially magnetised PMs : components of magnetization vector [15]	16
2.4	Radial magnetic flux density in the center of internal PM region for a different number of harmonics	23
2.5	Dual Halbach topology : Radial magnetic flux density as a function of r with $z = 0$	24
2.6	Internal PM region : Magnetic flux density as a function of z with $r = 27.5 [mm]$	25
2.7	External PM region : Magnetic flux density as a function of z with $r = 92.5 [mm]$	25
2.8	Air gap region : Magnetic flux density as a function of z with $r = 60 [mm]$	26
2.9	Internal radially magnetised PM array topology : Radial magnetic flux density as a function of r with $z = \tau_p/4$	27
2.10	Internal radially magnetised PM array topology : Axial magnetic flux density as a function of r with $z = \tau_p/4$	27
2.11	Internal PM region : Magnetic flux density as a function of z with $r = 35 [mm]$	27
2.12	Air gap region : Magnetic flux density as a function of z with $r = 75 [mm]$	28
2.13	Internal axially magnetised PM array topology : Radial magnetic flux density as a function of r with $z = \tau_p/4$	29
2.14	Internal axially magnetised PM array topology : Axial magnetic flux density as a function of r with $z = \tau_p/4$	29
2.15	Internal PM region : Magnetic flux density as a function of z with $r = 35 [mm]$	30
2.16	Air gap region : Magnetic flux density as a function of z with $r = 75 [mm]$	30
3.1	Structure of the TPMA with single-phase windings [2]	32
3.2	Thrust generated by single-phase winding TPMA	34
3.3	Structure of a TPMA with double-phase windings [2]	34
3.4	Thrust variation generated by double-phase winding TPMA	36

3.5	Structure of a TPMA with three-phase windings [2]	37
3.6	Two different starting positions	37
3.7	Fundamental force as a function of the starting position x	39
3.8	Thrust variation generated by three-phase winding TPMA	39
4.1	Vector representation of the PSO [24]	42
4.2	Convergence of the thrust	45
4.3	Radial magnetic flux density as a function of z with $r = 78.65595$ [mm]	46
4.4	Thrust variation generated by a TPMA with PSO dimensions	46
4.5	Convergence of the problem variables during the iterations	49
4.6	Convergence of the objective functions	50
4.7	Radial magnetic flux density as a function of z with $r = 72.32935$ [mm]	51
4.8	Thrust variation generated by a TPMA with VEPSO dimensions	51
5.1	Dirichlet boundary condition [30]	52
5.2	Illustration of end effects for a finite length TPMA [3]	53
5.3	Structure of the TPMA with infinitely long back iron and with series PM-array	54
5.4	Active suspension model of 1/4 train's car [34]	55
5.5	Fundamental force as a function of current density	56
5.6	Block diagram of an electromagnetic active suspension [35]	56

List of Tables

2.1	Principal Dimensions of the Dual Halbach TPMA	23
2.2	Principal Dimensions of the internal radially magnetised PM array TPMA	26
2.3	Principal Dimensions of the internal axially magnetized PM array TPMA	28
3.1	Results obtained for the different types of winding	40
4.1	Dimensions of the dual Halbach array TPMA obtained after PSO	45
4.2	Dimensions of the dual Halbach array TPMA obtained after VEPSO	50

List of Abbreviations

DOF Degrees Of Freedom.

FEM Finite Element Method.

GA Genetic Algorithm.

MOO Multi-Objective Optimisation.

PM Permanent Magnet.

PSO Particle Swarm Optimisation.

SOO Single-Objective Optimisation.

TPMA Tubular Permanent Magnet Actuator.

VEPSO Vector Evaluated Particle Swarm Optimisation.

Chapter 1

Introduction

1.1 Context of the project

With the ecology in a critical state right now, it is necessary for everyone to reduce their carbon footprint. In Belgium, the target for reducing the carbon footprint of each citizen is 55%. A non-negligible part of this carbon footprint comes from transport, about 22% [1]. The best way to reduce our carbon footprint from transport is to use public transport such as the train. Thus an increase in the number of rail users is expected in the coming years. It is therefore necessary to improve this transport service and make it even more environmentally friendly.

These improvements require the development of rail technologies. One of the major developments would be the complete electrification of the vehicle by replacing the hydraulic elements with electrical systems. This replacement would firstly allow the simplification of certain systems, given that the hydraulic elements are often quite complex, and secondly to reduce the energy consumption of the train. Two major systems still use hydraulic elements: the braking system and the suspension system.

The study of this thesis deals with the replacement of the hydraulic dampers present in the suspension system by electromagnetic dampers. The most suitable electromagnetic damper technology for the case presented is the Tubular Permanent Magnet Actuator (TPMA). New functions are brought by this new technology.

- A reduction in consumption thanks in part to energy recovery.
- Electrification of the active suspension system.
- Active control of the pendulum when turning.
- Better adaptability to the mass of the train.
- Better filtering of road excitation and therefore better ride comfort

1.2 Description of the technology

TPMAs are directly derived from synchronous rotary machines. The rotary machine was transformed by being flattened, so that the rotary motion was transformed into a linear motion. This evolution is shown in Figure 1.1.

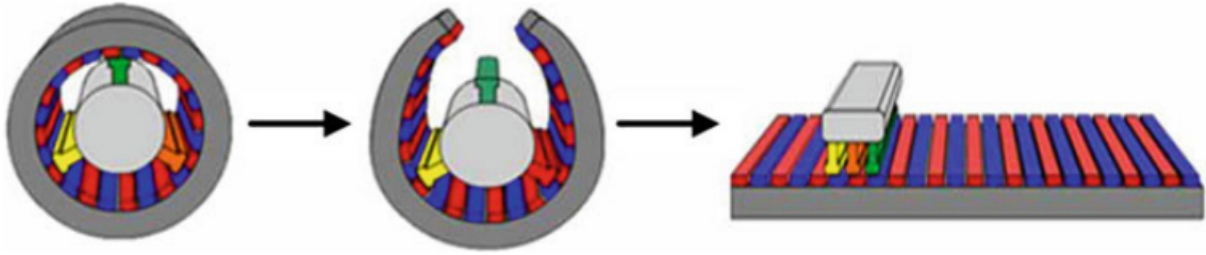


Figure 1.1: Evolution of rotary motor to linear machine [2]

This technology has many advantages [2]-[3]:

- It is a direct drive system so no intermediate transmission is necessary. Thus their efficiency is very high because there is no loss of energy due to an intermediate transmission.
- These linear machines are the ideal candidate for suspension. Indeed, they can achieve magnetic suspension to reduce friction and thus vibration between the stator and the mover as much as possible since there is no contact between the two.
- Since a linear motion is produced, there are no centrifugal forces so the translations produced can be extremely fast.
- As the link between the payload and the machine is direct, the inertia of the moving components is quite small, which improves the dynamic performance of the machine.

TPMAs thus consist of Permanent Magnet (PM)s which are mounted on the stator and an armature consisting of windings is mounted on the mover or vice versa. The basic principle of this linear machine is to transform the electrical energy injected into the windings into linear motion and therefore into mechanical energy. This linear movement is produced by the electromotive force produced by the interaction of the magnetic flux produced by the PMs and the current passing through the armature windings. As the name suggests, the TPMA has a tubular shape, i.e. the flat linear machine is rolled on itself to obtain this tubular shape. This tubular shape allows a better use of the machine's volume and thus obtains better performances.

A complete model of the TPMA is shown in Figure 1.2. It can be seen that in this case the PMs are placed on the mover and the windings are placed on the stator. In this case, the TPMA presented is single-sided such that it has only one array of PMs. A double-sided one is presented in the following. The model shown has a slotted armature as the windings are placed within the stator core slots. If the windings were mounted onto an iron core, the model would be equipped with a slotless frame. The TPMA housing is equipped with a cooling system to dissipate heat from the windings. Indeed, one of the critical points of the TPMA is its cooling because the windings tend to overheat, which leads to a loss of performance.

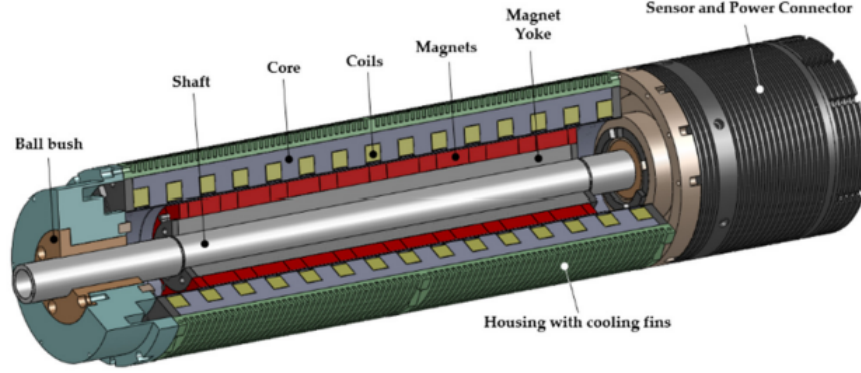


Figure 1.2: Complete structure of a TPMA [4]

1.3 The project

1.3.1 Objectives of the project

This thesis has three main objectives. The first one is to make a state of the art of the different existing TPMA topologies and to select the best one. This selection is done by means of a first analytical model on each of the interesting topologies. Once the first analytical model is developed, an objective comparison based on the electromagnetic behaviour of each of the topologies is carried out. At the end of this comparison, the best topology is selected.

The second objective is to develop a more advanced analytical model on the selected topology in order to know its performances such as the fundamental thrust or the ripple force. This advanced analytical model should also allow the selection of the type of winding used in the TPMA. Single-phase, double-phase and three-phase windings are therefore compared and the best winding type is selected.

The third objective is to optimise the dimensions of the selected topology. This optimisation must be carried out on the basis of the developed analytical model but also in order to optimise the performance of the TPMA. This optimisation should make it possible to obtain the dimensions of a possible TPMA test bench.

1.3.2 Structure of the thesis

The remainder of the thesis is organised as follows:

Chapter 1: The rest of the first chapter is dedicated to a state of the art of the most commonly used TPMA structures. Several choices are made such as the choice of the type of framework or the choice of topologies studied in the thesis.

Chapter 2: An analytical model for each of the topologies studied is developed. The objective is to obtain the magnetic field distribution behaviour for each of the topologies studied and to compare them. Thus this chapter contains the development of the solutions to the Laplace and Poisson equations from the Maxwell equations. The proof of the solutions is obtained by application of harmonic

expansion and by separation of variables.

Chapter 3: Analytical model to calculate the thrust produced by the TPMA topology selected in the previous chapter is developed. This development is based directly on the use of Laplace's equation which relates the current density injected into the armature coils and the magnetic flux density produced by the PMs. This chapter also develops the comparison between the different types of windings: single-phase, two-phase and three-phase. A comparison between these three types is made.

Chapter 4: With the topology and winding type chosen from the previous chapters, it is now possible to optimise the dimensions of the TPMA. First, a Particle Swarm Optimisation (PSO) is performed in order to obtain the dimensions of the TPMA that maximise the thrust produced. Then, the optimisation problem shifts to two objectives: maximizing the thrust and minimizing the ripple force. Thus a Vector Evaluated Particle Swarm Optimisation (VEPSO) is performed to obtain the dimensions of the TPMA that optimise the Multi-Objective Optimisation (MOO) problem.

Chapter 5: This chapter focuses with the improvements to be considered as well as the further study of the TPMA topology proposed. Thus, several improvements on the analytical model are suggested in order to obtain even more realistic performances. Then an introduction to the dynamic model and the integration of the TPMA as a component of a suspension system are developed.

Chapter 6: A conclusion summarising the main results of this thesis is made in this last chapter.

1.3.3 State of art

Several structural designs are shown in Figure 1.3. It can be seen that a TPMA is composed, in the vast majority of cases, of one or more rows of PMs and an armature composed of current coils. Thus there is a large variety of TPMA topologies.

Indeed, it is possible to place the PM layer on the outside or on the inside. This will have an impact on the magnetic flux density inside the TPMA which will affect its performance. It is preferable to choose to place the PM on the inner layer in order to increase the magnetic field intensity inside the TPMA and thus improve its performance. Thus internal magnet topologies are the most commonly used.

Then it is possible to choose the magnetisation of the magnets. This magnetisation is very important in the design of the TPMA as it directly influences the evolution of the magnetic field density inside the TPMA. Three types of magnetisation are used, radial, axial and Halbach.

Then it is also possible to choose which of the armature or the PM row is the stator or the mover. It is preferable to choose the armature as the mover in order to reduce the mass of the moving part. Thus it is possible to classify the mover into two categories: slotted one and slotless one. These two categories are illustrated in Figure 1.9. Slotted armatures have the great advantage of producing a higher force density. Unfortunately they have two major drawbacks. The first is a loss of energy caused by eddy currents in the soft iron between the windings. The second and more significant drawback is

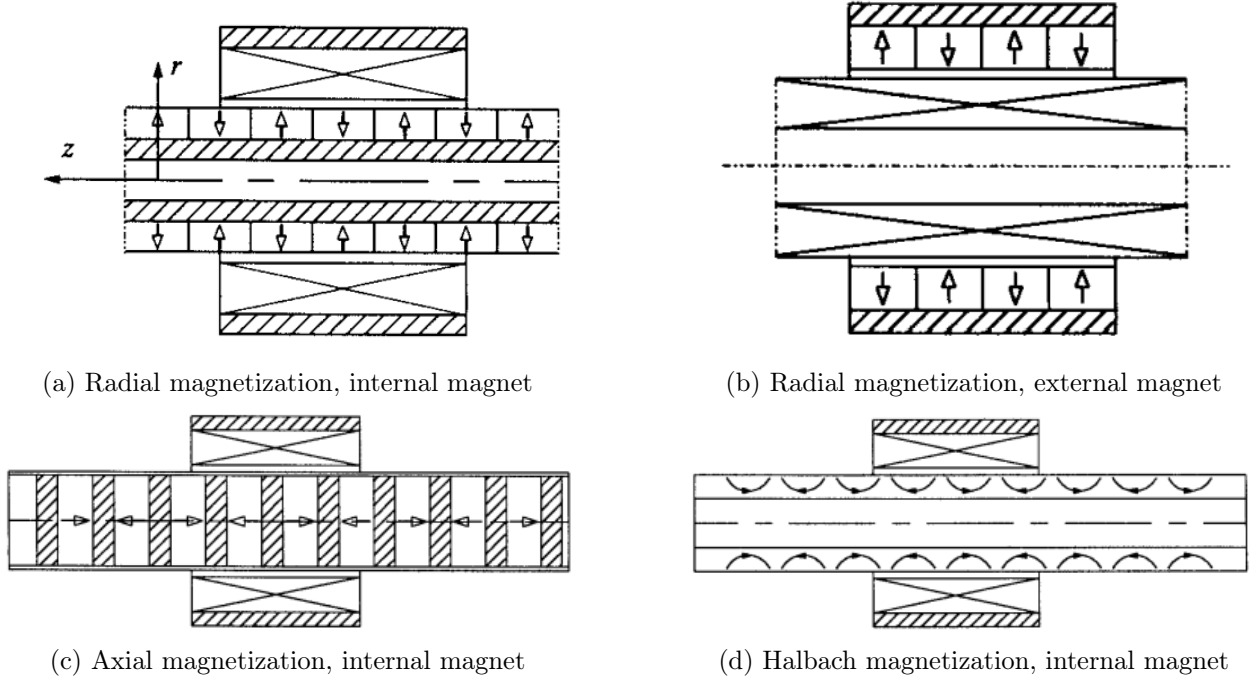


Figure 1.3: Most commonly used TPMA topologies [5]

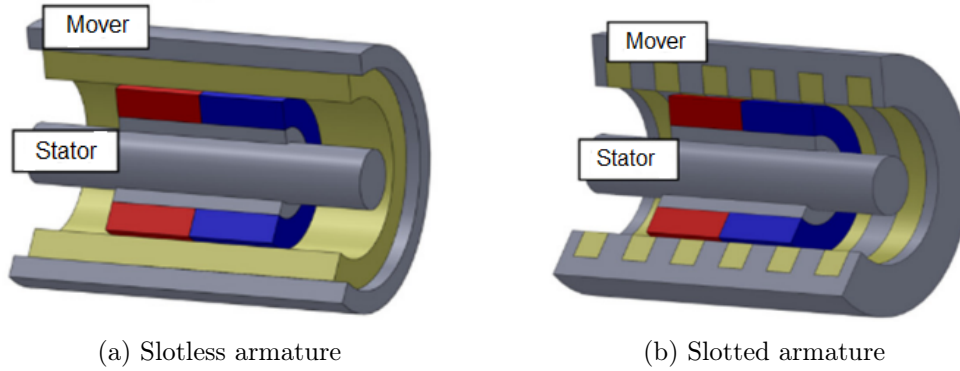


Figure 1.4: Slotless and Slotted armature topologies [4]

the tooth ripple cogging effect. It can be defined as a magnetic disturbance force that is caused by the attraction between the mover and the PMs, it is illustrated in Figure 1.5. This force is amplified when there is the presence of teeth as on slotted armatures. The effect is uniquely dependent on the relative position between the PMs and the mover [7]. Thus when the stator and mover teeth are aligned, the net cogging force is zero. However, when they are not aligned, the axial force produced by the magnetic attraction between the mover teeth and the stator magnets is no longer zero. Thus the mover tends to return to the position with the minimum energy, which is the position where the cogging force is zero. This phenomenon is repeated periodically, causing the TPMA's thrust force to fluctuate and thus reducing its performance. The period of these fluctuations is equal to the slot pitch of the teeth [6].

In contrast, slotless armatures produce slightly less force density but this is not altered by the tooth ripple cogging effect [2]. Thus slotless armatures are most often chosen for dynamic applications such as the use of TPMA as a railway suspension. Therefore the armatures are still considered as slotless in the rest of the study.

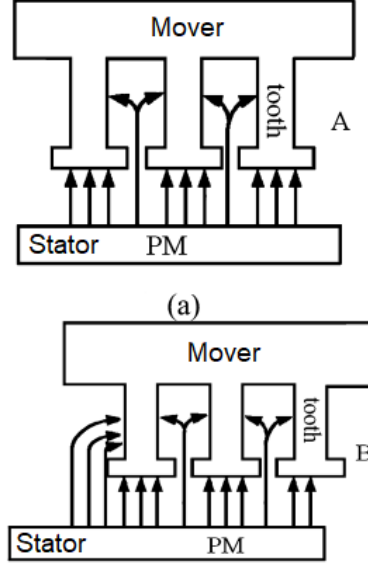


Figure 1.5: Cogging force produced by the offset between the mover teeth and the PMs [6]

1.3.4 Topologies studied in the thesis

As previously stated, many different designs exist. However, three topologies are the most commonly used for various applications and will therefore be studied in the remainder of this study.

The first topology studied consists of a single internal array of PMs. These PMs are radially magnetised, this topology is illustrated in Figure 1.6. With this topology, two regions are present. The first region is the air gap region where the armature is present. The second region is the PM region. We can notice that 5 parameters allow to define the global geometry of the TPMA: The three radii R_1 , R_2 and R_3 , the pole pitch τ_p and the width of radially magnetized PM τ_r . The air gap between the armature and the PMs is denoted by g , its value is fixed at 1 [mm].

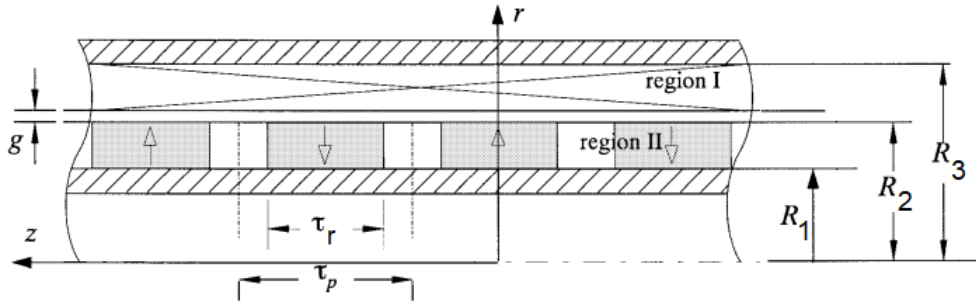


Figure 1.6: Scheme of radially magnetized PM topology [5]

The second topology studied also consists of a single internal array of PMs but this time the PMs are magnetised axially. This results in a change in the evolution of the magnetic flux density within the TPMA. The performance and behaviour of the TPMA is different compared to the first topology. The second topology is shown in Figure 1.7, the same regions and the same geometric parameters as for the first topology are present. Only the parameter τ_m changes with respect to the first topology and it represents the width of the axially magnetised PMs.

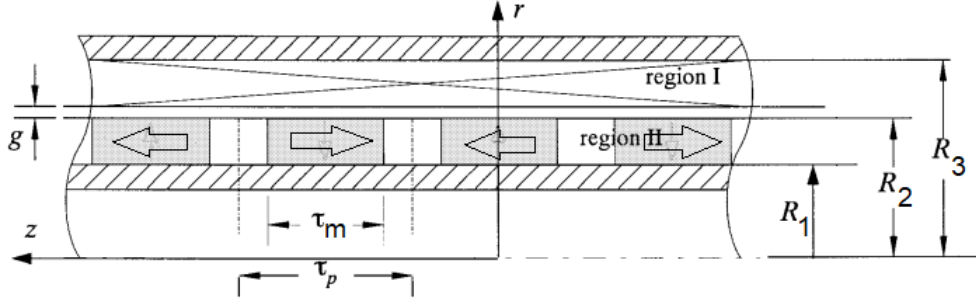


Figure 1.7: Scheme of axially magnetized PM topology [5]

Finally, the third topology studied is the dual Halbach array topology. It is shown in Figure 1.8. It

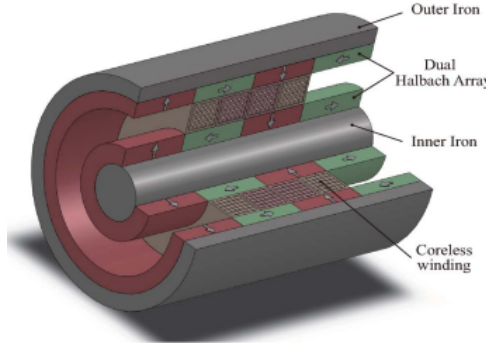


Figure 1.8: Structure of dual Halbach array TPMA [8]

can be seen that it differs from the two previous ones in two aspects. Firstly, it has two rows of PMs to amplify the magnetic flux density in the air gap region. Secondly, the polarization pattern of each array of the PMs is different from the other two topologies as it combines both radially magnetised magnets and axially magnetised PMs. This pattern is called a quasi-Halbach array and aims to produce a magnetic field as close as possible to that which would be produced by an ideal Halbach array. The quasi-Halbach magnetisation is preferred to the ideal Halbach as it is very complicated to manufacture [9].

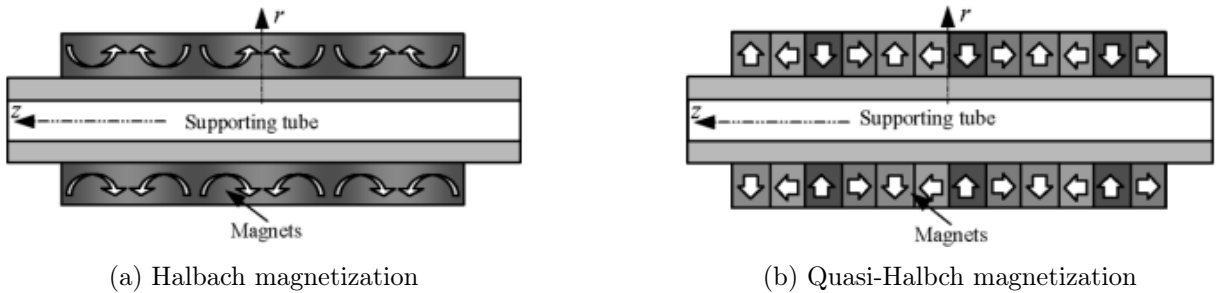


Figure 1.9: Polarization pattern arrays of TPMA [9]

This magnet pattern has two interesting properties. The first is that the magnetic field is sinusoidally distributed in the air gap region. The second is that it has a self-shielding property. That is, the magnetic field is intensified on one side of the row (air gap region) and is practically cancelled out on the other side (towards the back iron part). This is due to the superposition of the field produced by the radially magnetised PMs and the axially magnetised PMs as shown in Figure 1.10 [10].

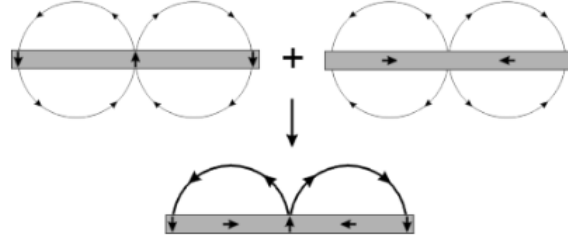


Figure 1.10: One-sided flux [11]

The geometry of this topology is shown in Figure 1.11. It can be seen that three regions are present. Region 1 is the air gap region, Region 2 is the external PM region and Region 3 is the internal PM region. Given the presence of an additional region, it is necessary to introduce an additional radius. Another parameter to be taken into account is the proportion of radially magnetised PM in the pole pitch. It is noted $\alpha = \tau_r / \tau_p$.

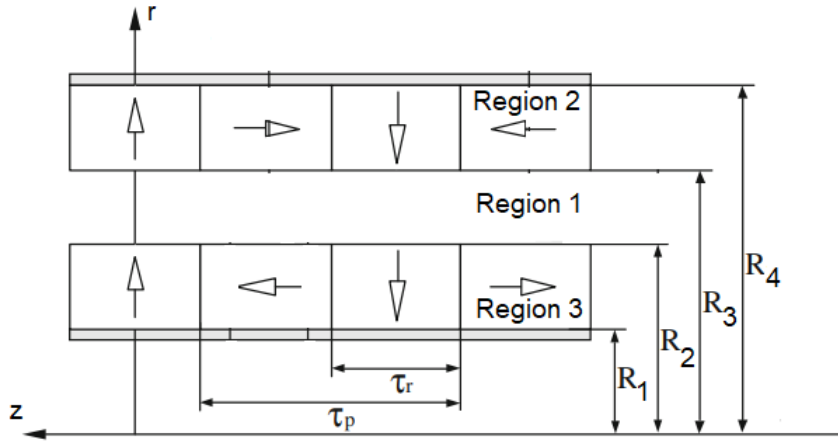


Figure 1.11: Scheme of Halbach magnetized PM topology

Chapter 2

Analytical Model of Magnetic field

In order to describe the performance of the actuator it is important to establish a model. This model must take into account the geometrical parameters as well as the topology of the actuator. Several models are possible and each has its positive and negative points.

Firstly, a finite element model is one of the most widely used choices. It allows non-linear phenomena such as induced currents in the winding to be taken into account [2]. It also allows to take into account the edge effects that are detrimental to the dynamic behaviour of the actuator. Unfortunately, it is not suitable for a parametric study of the geometric dimensions of the problem. Indeed, the simulations are too time-consuming.

Next, it is possible to perform the lumped equivalent circuit to determine the magnetic field in the actuator. This circuit allows for analytical relationships between the geometric parameters of the problem and the performance of the actuator, which lends itself well to optimisation. The strong point of this circuit is that it takes into account the armature reaction effect. Unfortunately, this method becomes inaccurate when the path of the field lines is too complex [12].

Finally, in order to obtain a sufficiently accurate model that is not too time consuming, it is possible to establish an analytical model based on the fact that the solutions are characterised by series expansions. These series expansions are established through harmonic functions. This is the most suitable model for the study to be conducted. Indeed, it allows to establish analytical relationships between the geometrical parameters of the problem and the actuator performance. This will allow the impact of these parameters to be studied and the design of the actuator to be optimised according to the desired performance [2].

2.1 Assumptions

Before starting the mathematical development of the analytical model, it is important to state the assumptions made about the model. The assumptions that are made are intended to simplify the model and its study. The assumptions made are as follows [13]

- Back iron parts have an infinite permeability.
- The end effects are neglected because the TPMA is considered infinitely long.
- Eddy currents in stator and mover are ignored.

2.2 Governing equations of flux field

The purpose of this section is to define the expression for the flux density within the actuator. In a first step, the governing equations will be described using the theory of magnetostatics. These equations are common to all actuator topologies described in the following sections. First, using Gauss' theorem in its integral form

$$\int_S \mathbf{B}(\mathbf{r}) \cdot d\mathbf{S} = 0 \quad (2.1)$$

where \mathbf{r} is the position vector in cylindrical coordinates. then using the divergence theorem

$$\int_S \mathbf{B}(\mathbf{r}) \cdot d\mathbf{S} = \int_V (\nabla \cdot \mathbf{B}) dV = 0 \quad (2.2)$$

it is possible to obtain the differential form of Gauss' theorem

$$\nabla \cdot \mathbf{B} = 0 \quad (2.3)$$

The Equation 2.3 shows that the magnetic flux density curves within the actuator are closed curves because there is no magnetic point charge [14]. Then the magnetic vector potential is defined thanks to the primitivisation theory of vector fields

$$\mathbf{B} = \nabla \times \mathbf{A} \quad (2.4)$$

where \mathbf{A} in the Equation 2.4 is the magnetic vector potential and we can see that this vector respects the Equation 2.3 since the divergence of the curl of a vector is always zero. Finally, the expression for the curl of the flux density can be rewritten as follows

$$\nabla \times \mathbf{B} = \nabla \times (\nabla \times \mathbf{A}) = \nabla (\underbrace{\nabla \cdot \mathbf{A}}_{=0}) - \nabla^2 \mathbf{A} = -\nabla^2 \mathbf{A} \quad (2.5)$$

this equation will be useful in the following developments.

2.2.1 Laplace's equation for the air gap region

In this region, the magnetic field is defined as

$$\mathbf{H}(\mathbf{r}) = \frac{\mathbf{B}(\mathbf{r})}{\mu_0} \quad (2.6)$$

where the permeability of air is taken to be equal to that of free space, $\mu_0 = 4\pi \times 10^{-7} \text{H/m}$. Then using the differential form of Ampere's theorem

$$\nabla \times \mathbf{H} = \mathbf{J} \quad (2.7)$$

where \mathbf{J} is the current density in the field which is zero in this region. Thus by combining the Equations 2.5, 2.6 and 2.7, the Laplace equation in the air gap is obtained as

$$\nabla^2 \mathbf{A}_1 = 0 \quad (2.8)$$

2.2.2 Poisson's equation for the permanent magnet region

In this region, the expression of the magnetic field is different because the magnetization vector present in the permanent magnets must be taken into account [14]. The relationship between flux density and magnetic field is then modified

$$\mathbf{B}_2 = \mu_0 \mu_r \mathbf{H}_2 + \mu_0 \mathbf{M} \quad (2.9)$$

where μ_r is the relative permeability of permanent magnets. The magnetization vector is obtained thanks to the remanence

$$\mathbf{M} = \mathbf{B}_{rem} / \mu_0 \quad (2.10)$$

Thus by combining the Equations 2.5, 2.7 and 2.9, the Poisson's equation in the permanent magnet region is obtained as

$$\nabla^2 \mathbf{A}_2 = -\mu_0 \nabla \times \mathbf{M} \quad (2.11)$$

where the current density is again zero in this region.

2.3 Solution to flux density distribution

2.3.1 Solution to Laplace's equation

In order to obtain the expression for the flux density distribution, it is necessary to solve the Equations 2.8 and 2.11. Since the actuator is tubular, the magnetic field distribution is axially symmetrical. This simplifies the expression of the potential vector, which now has only one component A_θ . This component is independent of the θ coordinate. This component is then a function of the independent variables r and z :

$$A_\theta = R(r)Z(z) \quad (2.12)$$

It is then possible to rewrite the Laplace Equation 2.8 by taking advantage of the axial symmetry

$$\frac{\partial^2 A_\theta}{\partial z^2} + \frac{\partial}{\partial r} \left(\frac{1}{r} \frac{\partial}{\partial r} (r A_\theta) \right) = 0 \quad (2.13)$$

Then applying the separation of variables described in the Equation 2.12

$$\frac{1}{R(r)} \frac{\partial^2 R(r)}{\partial r^2} + \frac{1}{R(r)r} \frac{\partial R(r)}{\partial r} + \frac{1}{Z(z)} \frac{\partial^2 Z(z)}{\partial z^2} - \frac{1}{r^2} = 0 \quad (2.14)$$

Since the variables r and z are independent, the third term of the Equation 2.14 must be a constant [2], this gives the following expression

$$\frac{1}{Z(z)} \frac{\partial^2 Z(z)}{\partial z^2} = k^2 \quad (2.15)$$

The Equation allows the Laplace Equation 2.14 to be rewritten according to two partial differential equations

$$\frac{\partial^2 Z(z)}{\partial z^2} - k^2 Z(z) = 0 \quad (2.16)$$

$$\frac{1}{R(r)} \frac{\partial^2 R(r)}{\partial r^2} + \frac{1}{R(r)r} \frac{\partial R(r)}{\partial r} + k^2 - \frac{1}{r^2} = 0 \quad (2.17)$$

There are three different solutions for the equations depending on the value of the constant k . However, only one solution must be kept. Indeed, since the actuator is tubular, the magnetic field is periodic and symmetrically distributed along the z axis. Thus the solution of the magnetic potential must also be symmetric. This solution is possible when the constant k fulfils the condition $k^2 < 0$ [15]. In this case, the following development is obtained

$$Z(z) = B_0 \cos(mz) + B_1 \sin(mz) \quad (2.18)$$

which gives the solution of the Equation 2.17 for the variable z . Concerning the Equation 2.16, it can be rewritten as follows by imposing the condition on the constant k

$$r^2 \frac{\partial^2 R(r)}{\partial r^2} + r \frac{\partial R(r)}{\partial r} + R(r) (k^2 r^2 - 1) = 0 \quad (2.19)$$

Then by defining m a real number and by posing $k = jm$ and $mr = x$, the Equation 2.19 is transformed into

$$x^2 \frac{\partial^2 R}{\partial x^2} + x \frac{\partial R}{\partial x} - (x^2 + 1) R = 0 \quad (2.20)$$

Combining the solution of the Equation 2.20 with the Equations 2.12 and 2.18, the solution of the magnetic potential is given by

$$A_\theta = [C_0 I_1(mr) + D_0 K_1(mr)] * [E_0 \cos(mz) + F_0 \sin(mz)] \quad (2.21)$$

where I_1 and K_1 are the first order modified Bessel functions of the first and the second kind defined as

$$I_\alpha(x) = \sum_{m=0}^{\infty} \frac{1}{m! \Gamma(m + \alpha + 1)} \left(\frac{x}{2}\right)^{2m+\alpha} \quad (2.22)$$

$$K_\alpha(x) = \frac{\pi}{2} \frac{I_{-\alpha}(x) - I_\alpha(x)}{\sin \alpha \pi} \quad (2.23)$$

The coefficients C_0 , D_0 , E_0 and F_0 must be determined using boundary conditions imposed by the actuator topology. Knowing that the z -component of the flux density is antisymmetric, the following condition can be derived: $B_z|_{z=0} = 0$ [2]. This boundary condition is common to all the topologies studied in this work and injected into the Equation 2.21 the values of the coefficients C_0 and D_0 can be obtained

$$C_0 = 0$$

$$D_0 = 0$$

Finally the general solution to the Laplace Equation is given by

$$A_\theta = \sum_{n=1}^{\infty} [a_n I_1(m_n r) + b_n K_1(m_n r)] \sin(m_n z) \quad (2.24)$$

where $m_n = \frac{(2n-1)\pi}{\tau_p}$, $a_n = E_0$ and $b_n = F_0$. As explained at the beginning of this chapter, the solution is well expressed using series expansions.

2.3.2 Solution to Poisson's equation

By applying the same transformation as for the Laplace equation, it is possible to rewrite the Poisson Equation in cylindrical coordinates

$$\frac{\partial A_\theta}{\partial z^2} + \frac{\partial}{\partial r} \left(\frac{1}{r} \frac{\partial}{\partial r} (r A_\theta) \right) = -\mu_0 \nabla \times \mathbf{M} \quad (2.25)$$

The homogeneous solution of the Equation 2.25 was obtained in the previous subsection

$$A_\theta = \sum_{n=1,2,\dots}^{\infty} [a_n I_1(m_n r) + b_n K_1(m_n r)] \sin(m_n z) \quad (2.26)$$

In order to obtain the particular solution of the Poisson equation, it is necessary that the magnetisation vector \mathbf{M} is expressed in harmonic expansions [2]. However, the magnetisation vector is specific to each of the topologies studied. Thus the particular solution is different from one topology to another.

2.3.2.1 Halbach array topology

In the case where the magnet topology is a Halbach array, then the magnetization vector has a radial component M_r and an axial component M_z as shown in Figure 2.1. Thus in cylindrical coordinates, the magnetisation vector can be expressed as

$$\mathbf{M} = M_r e_r + M_z e_z \quad (2.27)$$

As shown in the Figure 2.1, the radial component of the magnetization vector is an even non-continuous

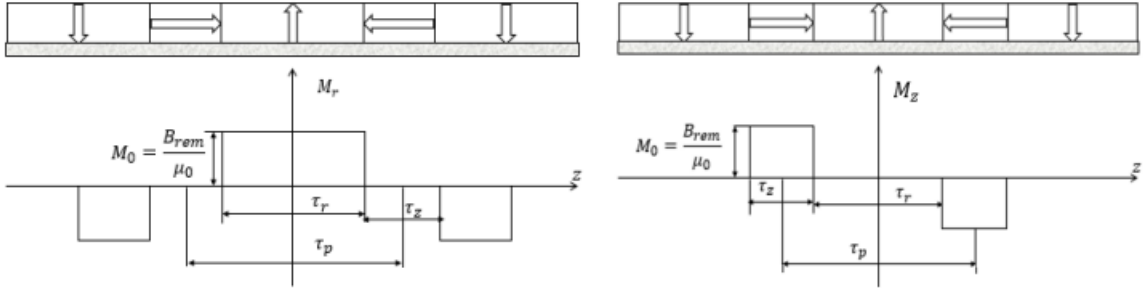


Figure 2.1: Halbach array : components of magnetization vector [15]

periodic function with a period of $2\tau_p$. Its harmonic expansion can be expressed in terms of the pole pitch τ_p , the width of the radially magnetised PMs τ_r and the remanence B_{rem}

$$M_r = \sum_{n=1}^{\infty} \frac{4B_{\text{rem}}}{(2n-1)\pi\mu_0} \sin\left(\frac{(2n-1)\pi\tau_r}{2\tau_p}\right) \cos(m_n z) \quad (2.28)$$

As shown in the Figure 2.1, the axial component is a non-continuous periodic odd function with a period of $2\tau_p$. Its harmonic expansion can be expressed in terms of the pole pitch, the width of the radially magnetised PMs and the remanence

$$M_z = -\sum_{n=1}^{\infty} \frac{4B_{\text{rem}}}{(2n-1)\pi\mu_0} \cos\left(\frac{(2n-1)\pi\tau_r}{2\tau_p}\right) \sin(m_n z) \quad (2.29)$$

Thus it is possible to transform the right-hand side of the Equation 2.25 using the Equations 2.28 and 2.29

$$-\mu_0 \nabla \times M = -\mu_0 \left(\frac{\partial M_r}{\partial z} - \frac{\partial M_z}{\partial r} \right) \quad (2.30)$$

$$\begin{aligned} &= \sum_{n=1,2,\dots}^{\infty} 4B_{rem} \frac{\sin \left[(2n-1) \frac{\pi}{2} \alpha \right]}{\tau_p} \sin(m_n z) \\ &= \sum_{n=1,2,\dots}^{\infty} P_n \sin(m_n z) \end{aligned} \quad (2.31)$$

where

$$\alpha = \frac{\tau_r}{\tau_p} \quad \text{and} \quad P_n = \frac{4}{\tau_p} B_{rem} \sin \left[(2n-1) \frac{\pi}{2} \alpha \right]$$

Then it is possible to obtain the total solution of the Poisson Equation by replacing the particular solution by

$$S(r, z) = R(r)Z(z) \quad (2.32)$$

and this must also be stated $\frac{1}{Z(z)} \frac{\partial^2 Z(z)}{\partial z^2} = -m_n^2$ in order to simplify the Poisson equation into

$$Z(z) = \sin(m_n z) \quad (2.33)$$

$$r^2 \frac{\partial^2 R(r)}{\partial r^2} + r \frac{\partial R(r)}{\partial r} - R(r) (m_n^2 r^2 + 1) = r^2 P_n \quad (2.34)$$

Finally, it is possible to transform the Equation 2.34, by posing $m_n r = x$ and $y = R(r) \frac{2m_n^2}{\pi P_n}$, into a modified Struve equation

$$x^2 \frac{\partial^2 y}{\partial x^2} + x \frac{\partial y}{\partial x} - y (x^2 + 1) = \frac{2x^2}{\pi} \quad (2.35)$$

the solution to which is

$$R(r) = \frac{\pi L_1(m_n r)}{2m_n^2} P_n \quad (2.36)$$

Using the results of Equations 2.33 and 2.36, the particular solution is obtained

$$S(r, z) = R(r)Z(z) = \frac{\pi L_1(m_n r)}{2m_n^2} P_n \sin(m_n z) \quad (2.37)$$

where L_1 is the modified Struve function of first order which is defined as [16]

$$L_\nu(m_n r) = \left(\frac{1}{2} m_n r \right)^{\nu+1} \sum_{k=0}^{\infty} \frac{\left(\frac{1}{2} m_n r \right)^{2k}}{\Gamma(k + \frac{3}{2}) \Gamma(k + \nu + \frac{3}{2})} \quad \text{with} \quad \Gamma(n) = (n-1)! \quad (2.38)$$

Using the result of the Equation 2.37, the magnetic potential in the PM region is then expressed

$$A_{2\theta} = \sum_{n=1}^{\infty} [a_{2n} I_1(m_n r) + b_{2n} K_1(m_n r)] \sin(m_n z) + \frac{1}{2} \frac{\pi L_1(m_n r)}{m_n^2} P_n \sin(m_n z) \quad (2.39)$$

Finally, we derive the expression for the radial and axial components of flux density in the air gap region using the Equation 2.24 and the definition of magnetic potential

$$B_{r1} = \sum_{n=1,2,\dots}^{\infty} -m_n [a_{1n} I_1(m_n r) + b_{1n} K_1(m_n r)] \cos(m_n z) \quad (2.40)$$

$$B_{z1} = \sum_{n=1,2,\dots}^{\infty} m_n [a_{1n} I_0(m_n r) - b_{1n} K_0(m_n r)] \sin(m_n z) \quad (2.41)$$

and in the region of the PMs using the Equation 2.39

$$B_{r2} = \sum_{n=1,2,\dots}^{\infty} -m_n \left[[a_{2n} I_1(m_n r) + b_{2n} K_1(m_n r)] \cos(m_n z) + \frac{1}{2} \frac{\pi L_1(m_n r)}{m_n^2} P_n \cos(m_n z) \right] \quad (2.42)$$

$$B_{z2} = \sum_{n=1,2,\dots}^{\infty} m_n \left[[a_{2n} I_0(m_n r) - b_{2n} K_0(m_n r)] \sin(m_n z) + \frac{1}{2} \frac{\pi L_0(m_n r)}{m_n^2} P_n \sin(m_n z) \right] \quad (2.43)$$

2.3.2.2 Radially magnetised PM array topology

With this magnet topology, the magnetisation vector has only a radial component as shown in the Figure 2.2. Thus in cylindrical coordinates, the magnetization vector can be expressed as

$$\mathbf{M} = M_r e_r \quad (2.44)$$

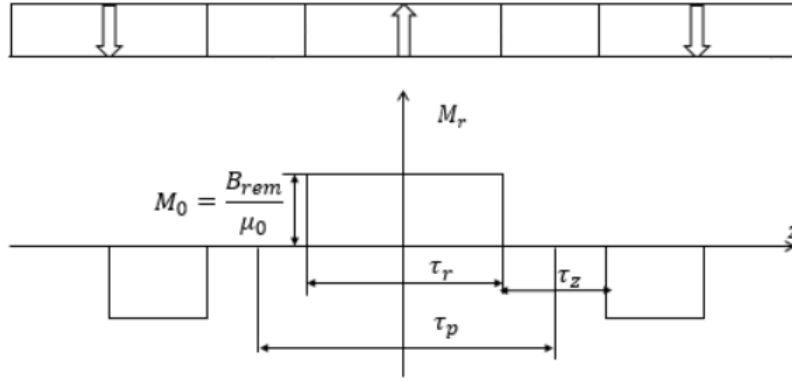


Figure 2.2: Radially magnetised PMs : components of magnetization vector [15]

The governing Equations 2.13 and 2.25 are identical to those used for the Halbach topology. The only point that changes is the expression of the magnetisation vector. Therefore the mathematical reasoning is identical to that of the previous subsection and will not be developed here. Only the results that change are described. The magnetization vector can be further expanded into Fourier series of the form [5]

$$M_r = \sum_{n=1,2,\dots}^{\infty} 4 (B_{\text{rem}}/\mu_0) \frac{\sin[(2n-1)\frac{\pi}{2}\alpha]}{(2n-1)\pi} \cos m_n z \quad (2.45)$$

so the expression for the magnetisation vector obtained in the equation allows the right-hand side to

be re-expressed in the Poisson Equation 2.25

$$\frac{\partial}{\partial z} \left(\frac{1}{r} \frac{\partial}{\partial z} (r A_{2\theta}) \right) + \frac{\partial}{\partial r} \left(\frac{1}{r} \frac{\partial}{\partial r} (r A_{2\theta}) \right) = \sum_{n=1}^{\infty} P_n \sin m_n z \quad (2.46)$$

As said before the solution of the Equation 2.46 is similar to the solution of the Equation 2.25, the reasoning is not detailed. Thus for the radially magnetised PM topology and after solving the Laplace equation for this topology and using the definition of the magnetic potential, the expression for the flux density in the air gap region is obtained

$$B_{1r}(r, z) = - \sum_{n=1}^{\infty} m_n [a_{1n} I_1(m_n r) + b_{1n} K_1(m_n r)] \cos(m_n z) \quad (2.47)$$

$$B_{1z}(r, z) = \sum_{n=1}^{\infty} m_n [a_{1n} I_0(m_n r) - b_{1n} K_0(m_n r)] \sin(m_n z) \quad (2.48)$$

and in the region of the internal PMs after solving Equation 2.46 [3]

$$B_{2r}(r, z) = - \sum_{n=1}^{\infty} m_n \left[a_{2n} I_1(m_n r) + b_{2n} K_1(m_n r) + \frac{\pi L_1(m_n r)}{2m_n^2} P_n \right] \cos(m_n z) \quad (2.49)$$

$$B_{2z}(r, z) = \sum_{n=1}^{\infty} m_n \left[a_{2n} I_0(m_n r) - b_{2n} K_0(m_n r) + \frac{\pi L_0(m_n r)}{2m_n^2} P_n \right] \sin(m_n z) \quad (2.50)$$

where R_1 is the internal radius of the PMs.

2.3.2.3 Axially magnetised PM array topology

With this magnet topology, the magnetisation vector has only an axial component as shown in the Figure 2.3. Thus in cylindrical coordinates, the magnetization vector can be expressed as

$$\mathbf{M} = M_z e_z \quad (2.51)$$

The magnetization vector can be further expanded into Fourier series of the form [17]

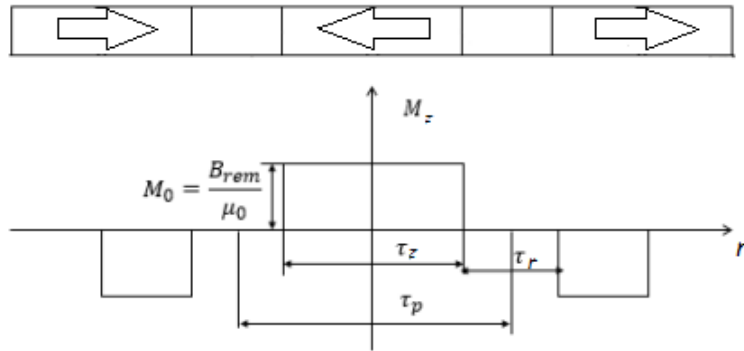


Figure 2.3: Axially magnetised PMs : components of magnetization vector [15]

$$M_z = - \sum_{n=1}^{\infty} \frac{4B_{\text{rem}}}{(2n-1)\pi\mu_0} \cos \left[\frac{(2n-1)\pi\tau_r}{2\tau_p} \right] \sin(m_n z) \quad (2.52)$$

However, it can be seen that the magnetisation vector for Axially magnetised PMs does not depend on r . Therefore, the curl of the magnetisation vector is zero since it contains only one component in z and this component is independent of r . Thus the right-hand side of the Poisson Equation 2.25 is zero using the result of Equation 2.30

$$\frac{\partial}{\partial z} \left(\frac{1}{r} \frac{\partial}{\partial z} (r A_{2\theta}) \right) + \frac{\partial}{\partial r} \left(\frac{1}{r} \frac{\partial}{\partial r} (r A_{2\theta}) \right) = 0 \quad (2.53)$$

The Equation 2.53 becomes a Laplace equation whose solution is similar to that described in Subsection 2.3.1. Thus for the axial magnet topology and after solving the Laplace equation for this topology and using the definition of the magnetic potential, the expression for the flux density in the air gap region is obtained

$$B_{1r} = \sum_{n=1}^{\infty} -m_n [a_{1n} I_1(m_n r) + b_{1n} K_1(m_n r)] \cos(m_n z) \quad (2.54)$$

$$B_{1z} = \sum_{n=1}^{\infty} m_n [a_{1n} I_0(m_n r) - b_{1n} K_0(m_n r)] \sin(m_n z) \quad (2.55)$$

and in the region of the internal PMs after solving Equation 2.53 [5]

$$B_{2r} = \sum_{n=1}^{\infty} -m_n [a_{2n} I_1(m_n r) + b_{2n} K_1(m_n r)] \cos(m_n z) \quad (2.56)$$

$$B_{2z} = \sum_{n=1}^{\infty} m_n [a_{2n} I_0(m_n r) - b_{2n} K_0(m_n r)] \sin(m_n z) \quad (2.57)$$

2.4 Boundary conditions

In order to determine the specific flux density distributions for each of the TPMA topologies and geometries, it is necessary to determine the coefficients of the series expansions. The boundary conditions are specific to each of the topologies presented in this study and are therefore treated separately. Nevertheless, the mathematical reasoning is similar from one topology to another. Thus the development for the dual Halbach array topology serves as a reference for the other topologies.

2.4.1 Dual Halbach array topology

In this topology, there are three distinct regions as shown in the Figure 1.11: the air gap region noted 1, the outer PM region noted 2 and the inner PM region noted 3. Therefore, it is necessary to determine 6 coefficients: a_{1n} , a_{2n} , a_{3n} , b_{1n} , b_{2n} and b_{3n} . These 6 coefficients are determined using 6 boundary conditions.

The first two boundary conditions are obtained by assuming that the back iron part has infinite permeability. Therefore, no field line escapes to the outside of the TPMA. For the region of the external PMs

$$\begin{aligned}
& H_{2z}|_{r=R_4} = 0 \\
\Leftrightarrow & \frac{B_{2z}}{\mu_0\mu_r}\bigg|_{r=R_4} - \frac{M_{2z}}{\mu_r}\bigg|_{r=R_4} = 0 \\
\Leftrightarrow & a_{2n}I_0(m_n R_4) - b_{2n}K_0(m_n R_4) = -L_0(m_n R_4) \frac{\pi P_n}{2m_n^2} + \frac{4B_{rem}}{(2n-1)\pi m_n} \cos\left(\frac{(2n-1)\pi\tau_r}{2\tau_p}\right) \quad (2.58)
\end{aligned}$$

and for the region of the internal PMs

$$\begin{aligned}
& H_{3z}|_{r=R_1} = 0 \\
\Leftrightarrow & \frac{B_{3z}}{\mu_0\mu_r}\bigg|_{r=R_1} - \frac{M_{3z}}{\mu_r}\bigg|_{r=R_1} = 0 \\
\Leftrightarrow & a_{3n}I_0(m_n R_1) - b_{3n}K_0(m_n R_1) = -L_0(m_n R_1) \frac{\pi P_n}{2m_n^2} - \frac{4B_{rem}}{(2n-1)\pi m_n} \cos\left(\frac{(2n-1)\pi\tau_r}{2\tau_p}\right) \quad (2.59)
\end{aligned}$$

The following two boundary conditions are obtained on the basis of continuity of the flux density and Ampere's theorem, the perpendicular component of the flux density is continuous between 2 adjacent media [18]. This condition is applicable to the boundary of the air gap region and the internal PM region

$$\begin{aligned}
& B_{3r}|_{r=R_2} = B_{1r}|_{r=R_2} \\
\Leftrightarrow & a_{3n}I_1(m_n R_2) + b_{3n}K_1(m_n R_2) - a_{1n}I_1(m_n R_2) - b_{1n}K_1(m_n R_2) = -L_1(m_n R_2) \frac{\pi P_n}{2m_n^2} \quad (2.60)
\end{aligned}$$

and to the boundary of the air gap region and the external PM region

$$\begin{aligned}
& B_{2r}|_{r=R_3} = B_{1r}|_{r=R_3} \\
\Leftrightarrow & a_{2n}I_1(m_n R_3) + b_{2n}K_1(m_n R_3) - a_{1n}I_1(m_n R_3) - b_{1n}K_1(m_n R_3) = -L_1(m_n R_3) \frac{\pi P_n}{2m_n^2} \quad (2.61)
\end{aligned}$$

The last two boundary conditions are again obtained using the principle of continuity between two media: the tangential component of the magnetic field is continuous at the boundary of two media

when the surface current is zero (which is the case here) [18]. This condition applies to the boundary of the air gap region and the internal PM region

$$\begin{aligned}
& H_{3z}|_{r=R_2} = H_{1z}|_{r=R_2} \\
\Leftrightarrow & \frac{B_{3z}}{\mu_0\mu_r}|_{r=R_2} - \frac{M_{3z}}{\mu_r}|_{r=R_2} = \frac{B_{1z}}{\mu_0}|_{r=R_2} \\
\Leftrightarrow & a_{3n}I_0(m_n R_2) - b_{3n}K_0(m_n R_2) - \mu_r a_{1n}I_0(m_n R_2) + \mu_r b_{1n}K_0(m_n R_2) \\
& = -L_0(m_n R_2) \frac{\pi P_n}{2m_n^2} - \frac{4B_{rem}}{(2n-1)\pi m_n} \cos\left(\frac{(2n-1)\pi\tau_r}{2\tau_p}\right)
\end{aligned} \tag{2.62}$$

and to the boundary of the air gap region and the external PM region

$$\begin{aligned}
& H_{2z}|_{r=R_3} = H_{1z}|_{r=R_3} \\
\Leftrightarrow & \frac{B_{2z}}{\mu_0\mu_r}|_{r=R_3} - \frac{M_{2z}}{\mu_r}|_{r=R_3} = \frac{B_{1z}}{\mu_0}|_{r=R_3} \\
\Leftrightarrow & a_{2n}I_0(m_n R_3) - b_{2n}K_0(m_n R_3) - \mu_r a_{1n}I_0(m_n R_3) + \mu_r b_{1n}K_0(m_n R_3) \\
& = -L_0(m_n R_3) \frac{\pi P_n}{2m_n^2} + \frac{4B_{rem}}{(2n-1)\pi m_n} \cos\left(\frac{(2n-1)\pi\tau_r}{2\tau_p}\right)
\end{aligned} \tag{2.63}$$

Putting the Equations 2.58 - 2.63 into a matrix system $\mathbf{AX} = \mathbf{F}$

$$\begin{bmatrix} 0 & 0 & A_{13} & A_{14} & 0 & 0 \\ 0 & 0 & 0 & 0 & A_{25} & A_{26} \\ A_{31} & A_{32} & A_{33} & A_{34} & 0 & 0 \\ A_{41} & A_{42} & A_{43} & A_{44} & 0 & 0 \\ A_{51} & A_{52} & 0 & 0 & A_{55} & A_{56} \\ A_{61} & A_{62} & 0 & 0 & A_{65} & A_{66} \end{bmatrix} \begin{bmatrix} a_{1n} \\ b_{1n} \\ a_{2n} \\ b_{2n} \\ a_{3n} \\ b_{3n} \end{bmatrix} = \begin{bmatrix} F_1 \\ F_2 \\ F_3 \\ F_4 \\ F_5 \\ F_6 \end{bmatrix} \tag{2.64}$$

where

$$\begin{aligned}
& A_{13} = I_0(m_n R_4); A_{14} = -K_0(m_n R_4); F_1 = -L_0(m_n R_4) \frac{\pi P_n}{2m_n^2} + \frac{4B_{rem}}{(2n-1)\pi m_n} \cos\left(\frac{(2n-1)\pi\tau_r}{2\tau_p}\right); \\
& A_{25} = I_0(m_n R_1); A_{26} = -K_0(m_n R_1); F_2 = -L_0(m_n R_1) \frac{\pi P_n}{2m_n^2} - \frac{4B_{rem}}{(2n-1)\pi m_n} \cos\left(\frac{(2n-1)\pi\tau_r}{2\tau_p}\right); \\
& A_{31} = -I_1(m_n R_3); A_{32} = -K_1(m_n R_3); A_{33} = I_1(m_n R_3); A_{34} = -K_1(m_n R_3); F_3 = -L_1(m_n R_3) \frac{\pi P_n}{2m_n^2}; \\
& A_{41} = -\mu_r I_0(m_n R_3); A_{42} = \mu_r K_0(m_n R_3); A_{43} = -I_0(m_n R_3); A_{44} = -K_0(m_n R_3); \\
& F_4 = -L_0(m_n R_3) \frac{\pi P_n}{2m_n^2} + \frac{4B_{rem}}{(2n-1)\pi m_n} \cos\left(\frac{(2n-1)\pi\tau_r}{2\tau_p}\right); \\
& A_{51} = -I_1(m_n R_2); A_{52} = -K_1(m_n R_2); A_{55} = I_1(m_n R_2); A_{56} = K_1(m_n R_2); F_5 = -L_1(m_n R_2) \frac{\pi P_n}{2m_n^2}; \\
& A_{61} = -\mu_r I_0(m_n R_2); A_{62} = \mu_r K_0(m_n R_2); A_{65} = I_0(m_n R_2); A_{66} = -K_0(m_n R_2); \\
& F_6 = -L_0(m_n R_2) \frac{\pi P_n}{2m_n^2} - \frac{4B_{rem}}{(2n-1)\pi m_n} \cos\left(\frac{(2n-1)\pi\tau_r}{2\tau_p}\right);
\end{aligned}$$

2.4.2 Radially magnetised PM array topology

With this magnet topology, there are only two regions present in the actuator as shown in the Figure 1.6: the first region is the air gap and the second is the internal PMs. Therefore, only 4 coefficients have to be determined: a_{1n} , a_{2n} , b_{1n} and b_{2n} . These coefficients are obtained by applying the same boundary conditions from the Subsection 2.4.1.

The first two boundary conditions are obtained by assuming that the back iron has infinite permeability. Therefore, no field line escapes to the outside of the TPMA. For the region of the internal PM.

$$\begin{aligned} H_{2z}|_{r=R_1} &= 0 \\ \Leftrightarrow B_{2z}|_{r=R_1} &= 0 \quad \text{since} \quad M_{2z} = 0 \end{aligned} \quad (2.65)$$

and in the air gap region

$$\begin{aligned} H_{1z}|_{r=R_3} &= 0 \\ \Leftrightarrow B_{1z}|_{r=R_3} &= 0 \quad \text{since} \quad M_{1z} = 0 \end{aligned} \quad (2.66)$$

The following is obtained by the fact that the perpendicular component of the flux density is continuous between two media

$$B_{1r}|_{r=R_2} = B_{2r}|_{r=R_2} \quad (2.67)$$

The latter is obtained by the continuity of the tangential component of the magnetic field intensity between two media when the surface current is zero

$$H_{1z}|_{r=R_2} = H_{2z}|_{r=R_2} \quad (2.68)$$

After developing the Equations 2.65 - 2.68, it is possible to put them in the form of a matrix system [5]

$$\begin{bmatrix} 0 & 0 & A_{13} & A_{14} \\ A_{21} & A_{22} & 0 & 0 \\ A_{31} & A_{32} & A_{33} & A_{34} \\ A_{41} & A_{42} & A_{43} & A_{44} \end{bmatrix} \begin{bmatrix} a_{1n} \\ b_{1n} \\ a_{2n} \\ b_{2n} \end{bmatrix} = \begin{bmatrix} F_1 \\ F_2 \\ F_3 \\ F_4 \end{bmatrix} \quad (2.69)$$

where

$$A_{13} = I_0(m_n R_1); A_{14} = -K_0(m_n R_1); F_1 = -L_0(m_n R_2) \frac{\pi P_n}{2m_n^2};$$

$$A_{21} = I_0(m_n R_3); A_{22} = -K_0(m_n R_3); F_2 = 0;$$

$$A_{31} = I_1(m_n R_2); A_{32} = K_1(m_n R_2); A_{33} = -I_1(m_n R_2); A_{34} = -K_1(m_n R_2); F_3 = L_1(m_n R_2) \frac{\pi P_n}{2m_n^2};$$

$$A_{41} = \mu_r I_0(m_n R_2); A_{42} = -\mu_r K_0(m_n R_2); A_{43} = -I_0(m_n R_2); A_{44} = K_0(m_n R_2); F_4 = L_0(m_n R_2) \frac{\pi P_n}{2m_n^2};$$

2.4.3 Axially magnetised PM array topology

With this magnet topology, there are only two regions present in the actuator as shown in the Figure 1.7: the first region is the air gap and the second is the internal PMs. Therefore, only 4 coefficients have to be determined: a_{1n} , a_{2n} , b_{1n} and B_0 . These coefficients are obtained using the same conditions as described in the previous Subsection 2.4.1. It should be noted that in this study, the width of the axially magnetised PMs is considered to be equal to the width of the magnet pitch: $\tau_z = \tau_p$. This consideration will allow to simplify the boundary conditions [5].

The first two boundary conditions are established by the assumption of infinite permeability of the back iron. In the PM region

$$\begin{aligned} H_{2z}|_{r=R_1} &= 0 \\ \Leftrightarrow \frac{B_{2z}}{\mu_0\mu_r}|_{r=R_1} - \frac{M_{2z}}{\mu_r}|_{r=R_1} &= 0 \end{aligned} \quad (2.70)$$

and in the air gap region

$$\begin{aligned} H_{1z}|_{r=R_3} &= 0 \\ \Leftrightarrow B_{1z}|_{r=R_3} &= 0 \quad \text{since } M_{1z} = 0 \end{aligned} \quad (2.71)$$

The following is obtained by the fact that the perpendicular component of the flux density is continuous between two media

$$B_{1r}|_{r=R_2} = B_{2r}|_{r=R_2} \quad (2.72)$$

The latter is obtained by the continuity of the tangential component of the magnetic field intensity between two media when the surface current is zero

$$H_{1z}|_{r=R_2} = H_{2z}|_{r=R_2} \quad (2.73)$$

After developing the Equations 2.70 - 2.73, it is possible to put them in the form of a matrix system with $\tau_z = \tau_p$ so $\tau_r = 0$

$$\begin{bmatrix} 0 & 0 & A_{13} & A_{14} \\ A_{21} & A_{22} & 0 & 0 \\ A_{31} & A_{32} & A_{33} & A_{34} \\ A_{41} & A_{42} & A_{43} & A_{44} \end{bmatrix} \begin{bmatrix} a_{1n} \\ b_{1n} \\ a_{2n} \\ b_{2n} \end{bmatrix} = \begin{bmatrix} F_1 \\ F_2 \\ F_3 \\ F_4 \end{bmatrix} \quad (2.74)$$

where

$$A_{13} = I_0(m_n R_1); A_{14} = -K_0(m_n R_1); F_1 = -\frac{4B_{\text{rem}}}{m_n(2n-1)\pi};$$

$$A_{21} = I_0(m_n R_3); A_{22} = -K_0(m_n R_3); F_2 = 0;$$

$$A_{31} = I_1(m_n R_2); A_{32} = K_1(m_n R_2); A_{33} = -I_1(m_n R_2); A_{34} = -K_1(m_n R_2); F_3 = 0;$$

$$A_{41} = \mu_r I_0(m_n R_2); A_{42} = -\mu_r K_0(m_n R_2); A_{43} = -I_0(m_n R_2); A_{44} = K_0(m_n R_2); F_4 = \frac{4B_{\text{rem}}}{m_n(2n-1)\pi};$$

2.5 Representation of results

In this section, graphs of the radial and axial components of the magnetic flux density of each topology are presented. The first objective is to validate the boundary conditions that have been set in Section 2.4. The second objective is to compare the evolution of the radial component within the air gap region for each of the topologies. Since the force produced by the TPMA depends only on this component, it constitutes a criterion for choosing between the different topologies. Similar dimensions are used so that the magnetic flux density is only influenced by the topology of the TPMA and not by its dimensions. The dimensions are chosen to approximate the dimensions of TPMA used in active railway suspensions [4].

The type of PM used for each topology are made of the same material which is sintered rare earth Neodymium Iron Boron *NdFeB35*. Their magnetic remanence is 1.2 [T] and their recoil permeability is $\mu_r = 1.0997$ [2]. The vacuum permeability is set to a value of $4\pi \times 10^{-7}$ [H/m].

2.5.1 Note on calculations involving Bessel functions

Before proceeding to the sections concerning the representation of the results obtained, it is important to mention the problems encountered during their implementation.

Indeed, the solutions of the magnetic flux densities are expressed by Fourier series. It is known that these series give a more precise solution when the number of harmonics tends towards infinity. However, there is the presence of the modified Bessel functions of the first kind and second kind I_n and K_n which complicates the solution of the magnetic flux density.

In fact, higher harmonic solutions cannot be obtained since the functions I_n and K_n become respectively extremely large or extremely small when the value of n , the number of harmonics, increases [19]. This results in an increasing deformation of the conditioning of the coefficient determination matrix as the value of n increases. Thus for too many harmonics, the values of the coefficients a_{in} and b_{in} become aberrant [20].

It is therefore necessary to create a stopping criterion on the value of n . This criterion must be adapted to each TPMA geometry since the value of the parameter r is involved in the argument of the functions I_n and K_n as expressed in Equation 2.42 for example.

The evolution of magnetic flux density in the center of internal PM region for the dual Halbach array TPMA will serve as an example to illustrate the importance of the number of harmonics in the Fourier series. The behaviour of B_{3r} is illustrated in Figure 2.4 for different values of n .

The correct behaviour of B_{3r} is obtained for $n = 14$ and is shown in Figure 2.4b. It is sufficient for the value of n to increase by 1 to see a completely aberrant behaviour of B_{3r} , as shown in Figure 2.4c and it becomes more and more aberrant as n increases as shown in Figure 2.4d. On the other hand, it can be noted that a too low value n leads to a loss of precision as too many harmonics are taken into account. The choice of the value of n is then a primordial choice.

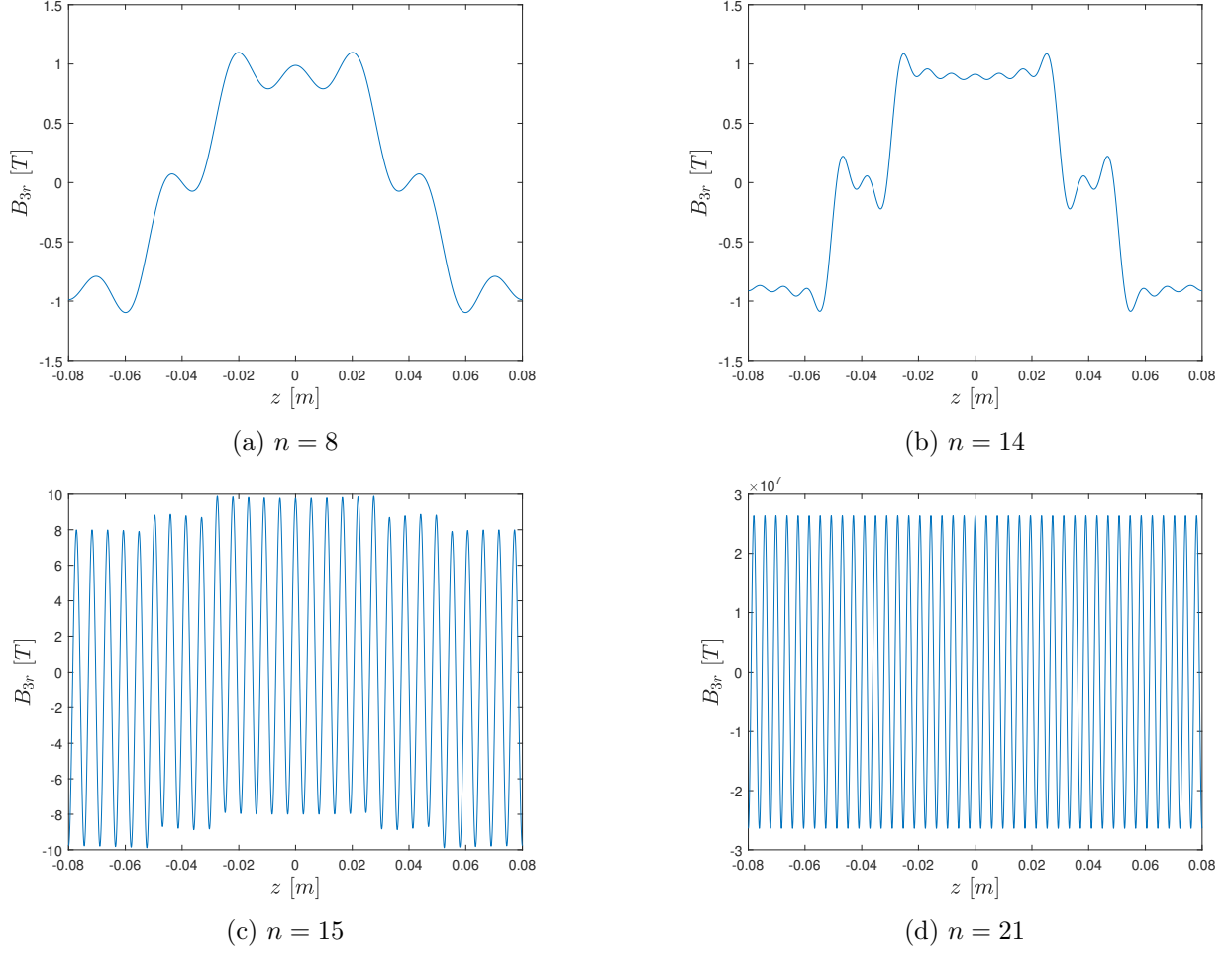


Figure 2.4: Radial magnetic flux density in the center of internal PM region for a different number of harmonics

2.5.2 Dual Halbach array topology

After implementing the analytical model, graphs of the magnetic flux densities for each region of the topology are plotted for a TPMA with the dimensions given in the Table 2.1.

Geometric Parameters	Value
Inner radius of internal PMs, R_1	20 [mm]
Outer radius of internal PMs, R_2	35 [mm]
Inner radius of external PMs, R_3	85 [mm]
Outer radius of external PMs, R_4	100 [mm]
Pole pitch, τ_p	80 [mm]
Width of radial magnets, τ_r	40 [mm]

Table 2.1: Principal Dimensions of the Dual Halbach TPMA

2.5.2.1 Validation of boundary conditions

For each of the regions, plots of the radial magnetic flux density as a function of r with the z -coordinate fixed at 0 are shown in the Figure 2.5.

The principle of continuity between the internal PM region and the air region expressed by Equation 2.60 is well respected and illustrated by Figures 2.6a and 2.8a. The same applies to the principle of continuity expressed by the Equation 2.60 and illustrated in Figures 2.8a and 2.7a.

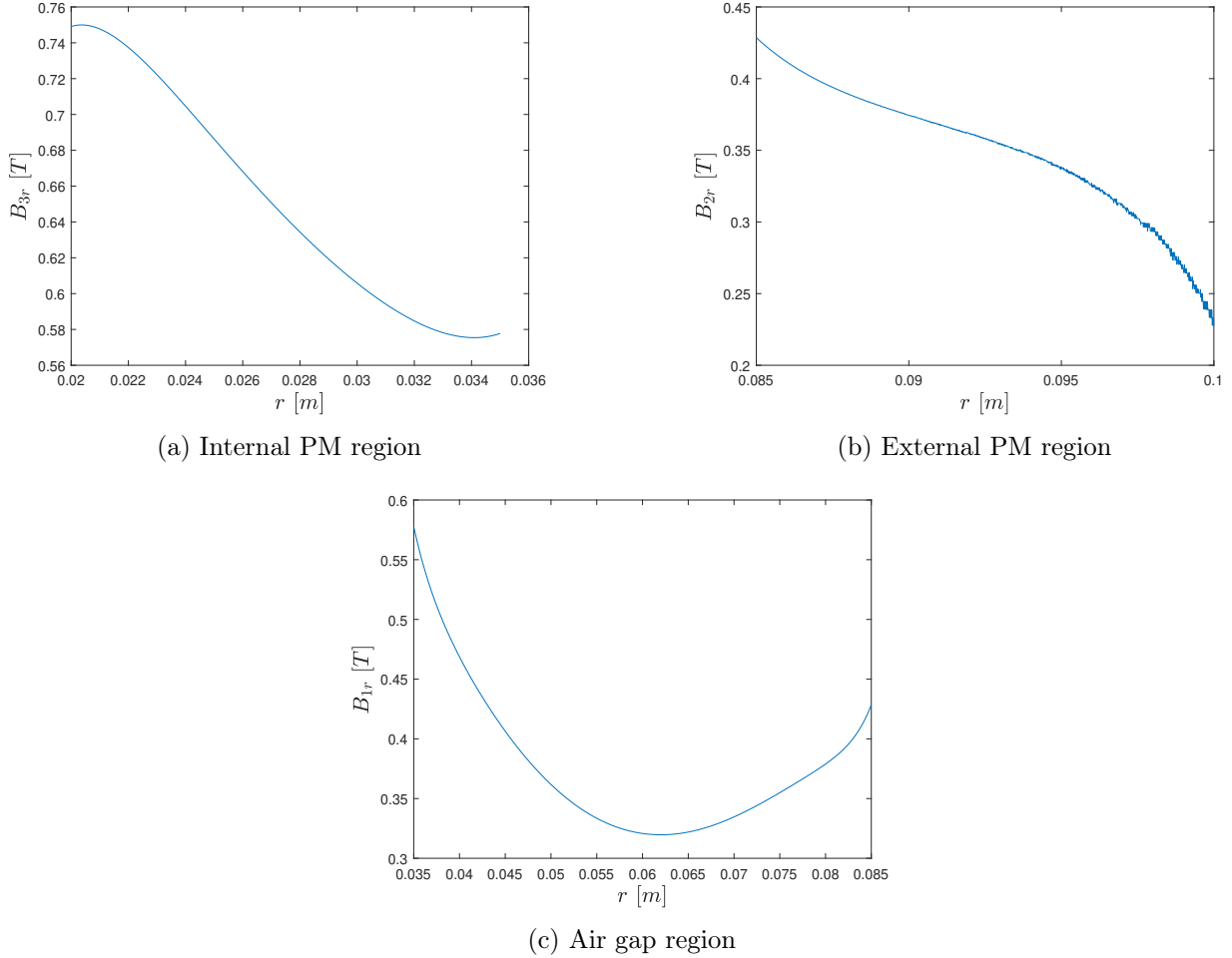
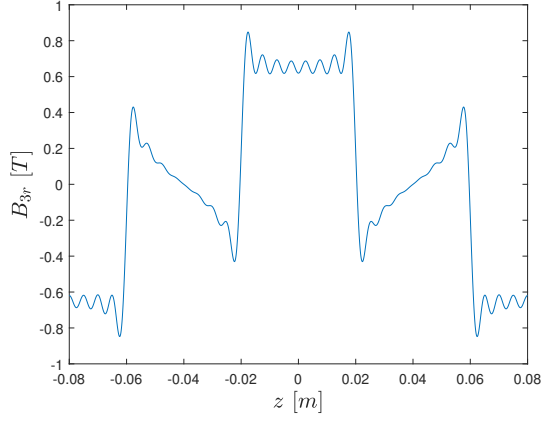


Figure 2.5: Dual Halbach topology : Radial magnetic flux density as a function of r with $z = 0$

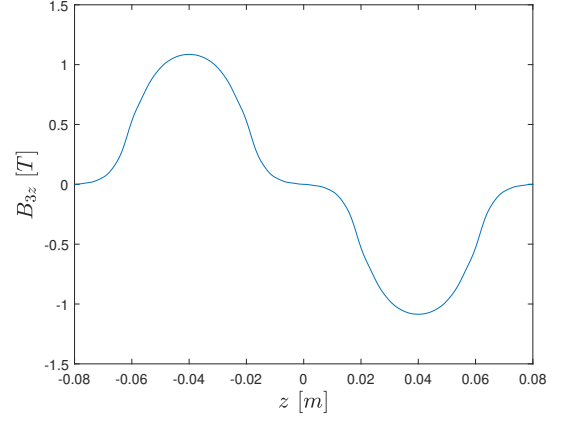
2.5.2.2 Magnetic flux density in the PM region

The Figure 2.6 shows the evolution of the magnetic flux density in the internal PM region with $r = (R_2 + R_1)/2$ and as a function of the axial position z . The Figure 2.7 shows the evolution of the magnetic flux density in the external PM region with $r = (R_3 + R_4)/2$ and as a function of the axial position z .

It can be seen that the variation of B_r and B_z within the two PM regions are consistent with the distribution of the magnetisation vectors M_r and M_z . Thus, the axial component of the magnetic flux density is odd-symmetric about $z=0$ [mm] while the radial component is even-symmetric. It can also be noted that the radial magnetic flux density in the outer PM region is lower than in the inner PM region because there is an increase in the cross-sectional area of flux lines [2].

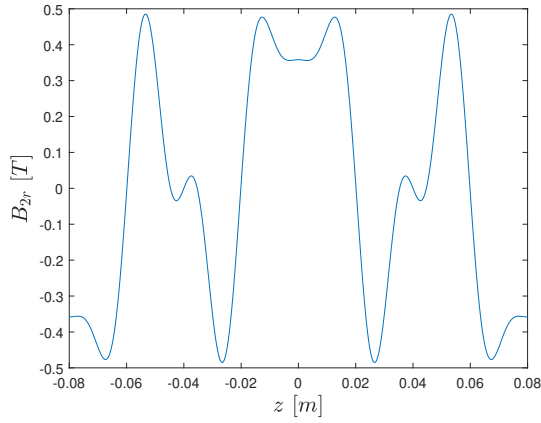


(a) Radial Component

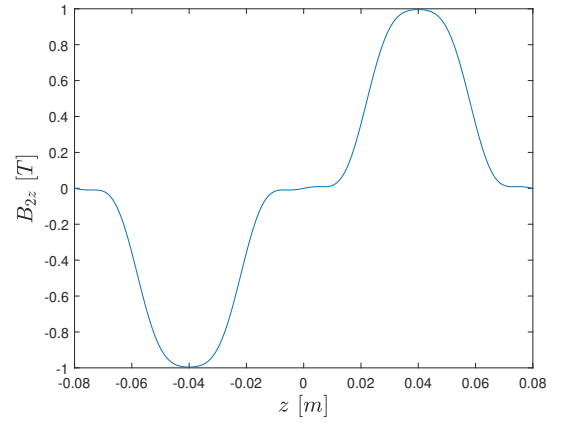


(b) Axial Component

Figure 2.6: Internal PM region : Magnetic flux density as a function of z with $r = 27.5$ [mm]



(a) Radial Component



(b) Axial Component

Figure 2.7: External PM region : Magnetic flux density as a function of z with $r = 92.5$ [mm]

The oscillations observed in the Figures 2.6 and 2.7 are caused by the analytical model. Indeed, when calculating the a_{in} and b_{in} coefficients, the Bessel functions are involved which causes instabilities. These instabilities occur for higher $(2n - 1)^{\text{th}}$ harmonics [3]

2.5.2.3 Magnetic flux density in the air gap region

The Figure 2.8 shows the evolution of the magnetic flux density in the air gap region with $r = (R_2 + R_3)/2$ and as a function of the axial position z . The Figure 2.8a shows that the radial flux density is fairly uniform in the air gap region, while the Figure 2.8b shows that the axial component of the magnetic flux density has peak point at half the pole pitch [2].

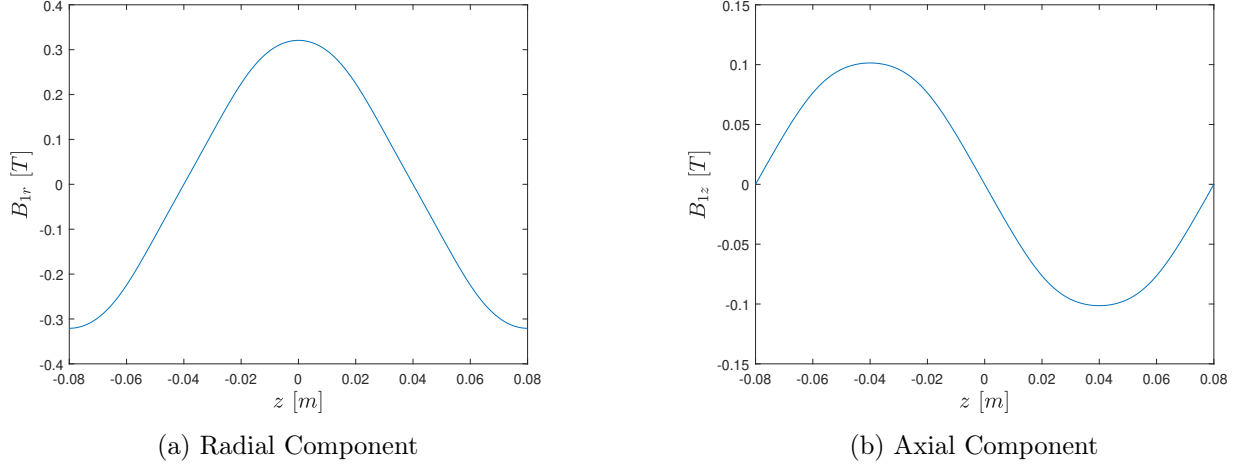


Figure 2.8: Air gap region : Magnetic flux density as a function of z with $r = 60$ [mm]

2.5.3 Radially magnetised PM array topology

After implementing the analytical model, graphs of the magnetic flux densities for each region of the topology are plotted for a TPMA with the dimensions given in the Table 2.2.

Geometric Parameters	Value
Inner radius of internal PMs, R_1	20 [mm]
Outer radius of internal PMs, R_2	50 [mm]
Outer radius of TPMA, R_3	100 [mm]
Pole pitch, τ_p	80 [mm]
Ratio of magnet pole-length to pole-pitch, α	1 [/]

Table 2.2: Principal Dimensions of the internal radially magnetised PM array TPMA

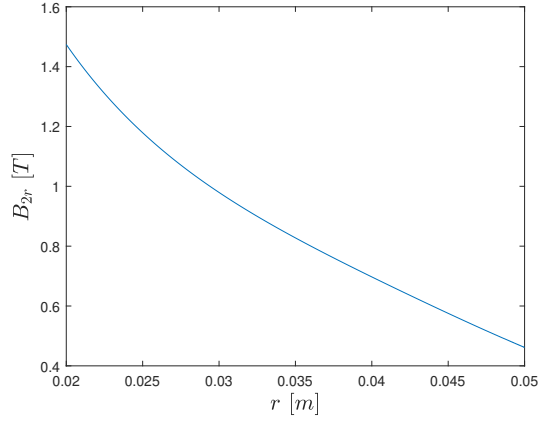
2.5.3.1 Validation of boundary conditions

The radial component of the magnetic flux density as a function of r and with $z = \tau_p/4$ is shown in Figure 2.9. In Figures 2.9a and 2.9b, it can be seen that the continuity condition expressed in the Equation 2.67 is well respected and that the value of B_r is identical in both regions for $r = R_2 = 50$ [mm].

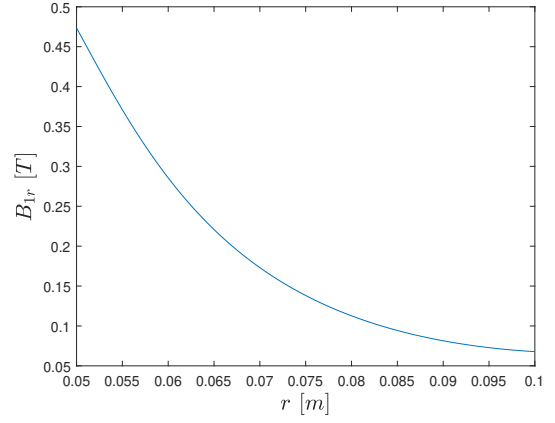
The axial component of the magnetic flux density as a function of r and with $z = \tau_p/4$ is shown in Figure 2.10. The conditions imposed in Equations 2.65 and 2.66 are satisfied since the value of B_z is zero for $r = R_1 = 20$ [mm] and $r = R_3 = 100$ [mm] as shown in Figures 2.10a and 2.10b. Finally we can notice that the value of B_z is not continuous between the two regions and makes a jump in value. This jump in value is due to the difference in permeability between the two media. Thus the value of B_{1z} is μ_r times greater than the value of B_{2z} .

2.5.3.2 Magnetic flux density in the magnetic region

The Figure 2.11 shows the evolution of the magnetic flux density in the internal PM region with $r = (R_1 + R_2)/2$ and as a function of the axial position z . Same observations as in Subsection 2.5.2.2 can be made on the results obtained in Figure 2.11.

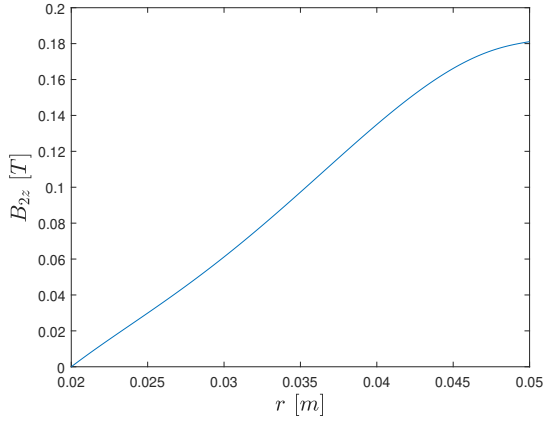


(a) Internal PM region

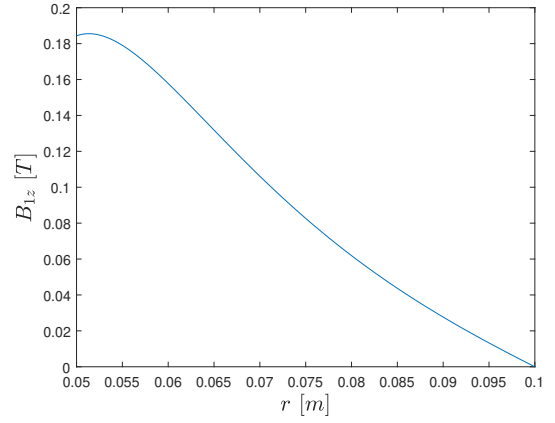


(b) Air gap region

Figure 2.9: Internal radially magnetised PM array topology : Radial magnetic flux density as a function of r with $z = \tau_p/4$

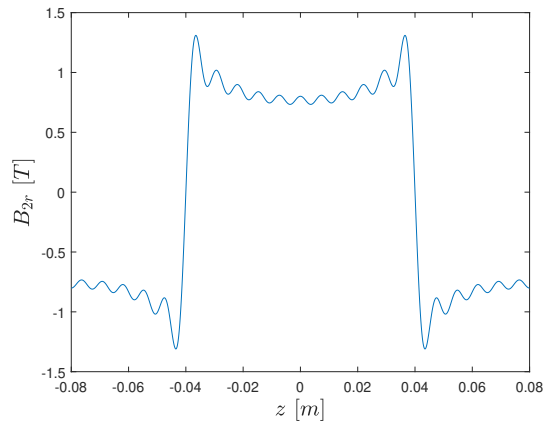


(a) Internal magnet region

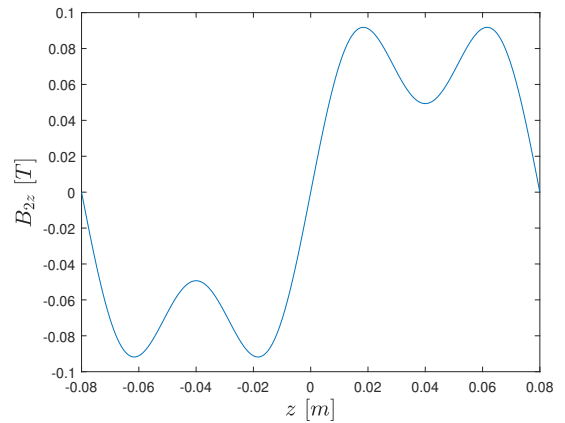


(b) Air gap region

Figure 2.10: Internal radially magnetised PM array topology : Axial magnetic flux density as a function of r with $z = \tau_p/4$



(a) Radial Component



(b) Axial Component

Figure 2.11: Internal PM region : Magnetic flux density as a function of z with $r = 35$ [mm]

2.5.3.3 Magnetic flux density in the air gap region

The Figure 2.12 shows the evolution of the magnetic flux density in the air gap region with $r = (R_2 + R_3)/2$ and as a function of the axial position z . Same observations as in Subsection 2.5.2.3 can be made on the results obtained in Figure 2.12. Nevertheless, it is interesting to add that the radial magnetic flux density at the centre of the air gap is lower for TPMA made up of radially magnetised PMs than for TPMA composed of dual Halbach array.

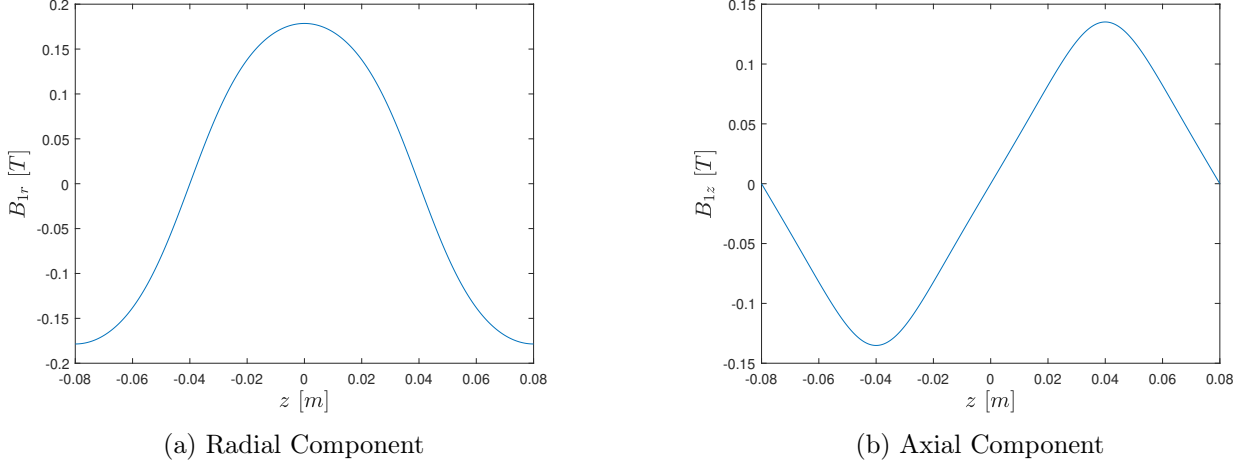


Figure 2.12: Air gap region : Magnetic flux density as a function of z with $r = 75$ [mm]

2.5.4 Axially magnetised PM array topology

After implementing the analytical model, graphs of the magnetic flux densities for each region of the topology are plotted for a TPMA with the dimensions given in the Table 2.3

Geometric Parameters	Value
Inner radius of internal PMs, R_1	20 [mm]
Outer radius of internal PMs, R_2	50 [mm]
Outer radius of TPMA, R_3	100 [mm]
Pole pitch, τ_p	80 [mm]
Width of the axially magnetised PM, τ_z	80 [mm]

Table 2.3: Principal Dimensions of the internal axially magnetized PM array TPMA

2.5.4.1 Validation of boundary conditions

The radial component of the magnetic flux density as a function of r and with $z = \tau_p/4$ is shown in Figure 2.13. In Figures 2.13a and 2.13b, it can be seen that the continuity condition expressed in the Equation 2.72 is well respected and that the value of B_r is identical in both regions for $r = R_2 = 50$ [mm].

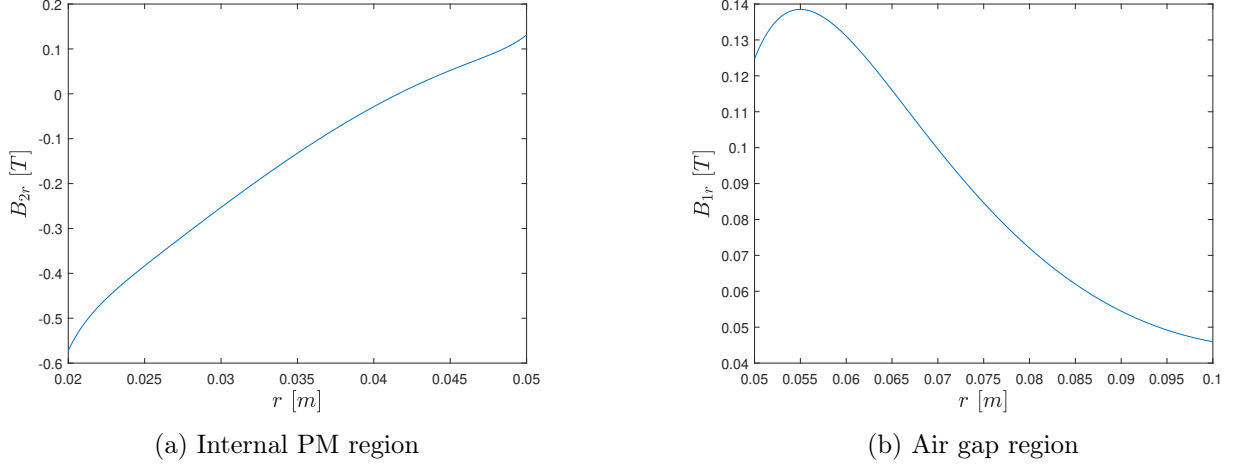


Figure 2.13: Internal axially magnetised PM array topology : Radial magnetic flux density as a function of r with $z = \tau_p/4$

The axial component of the magnetic flux density as a function of r and with $z = \tau_p/4$ is shown in Figure 2.14. The conditions imposed in Equation 2.71 is satisfied since the value of B_z is zero for $r = R_3 = 100$ [mm] in Figure 2.14b.

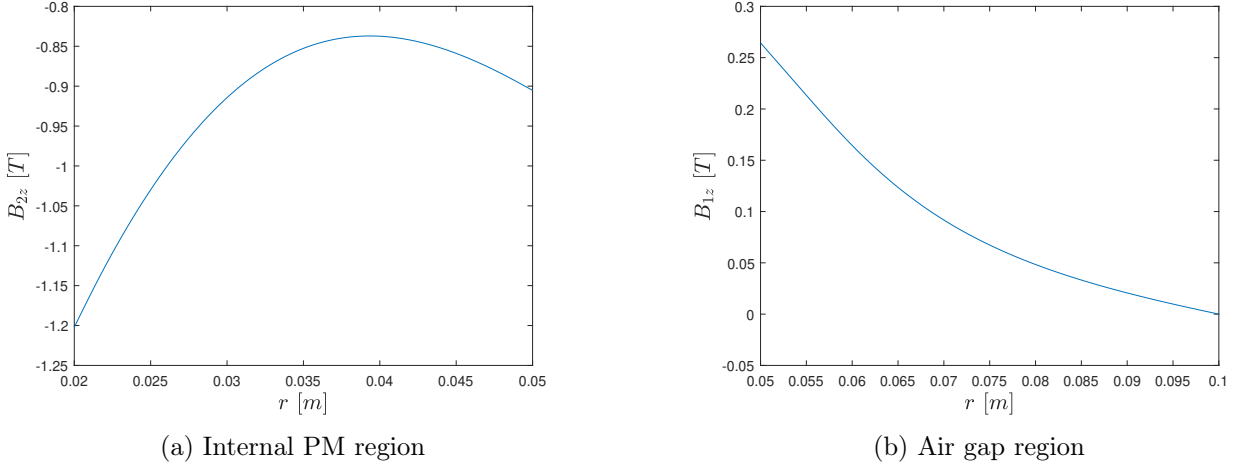
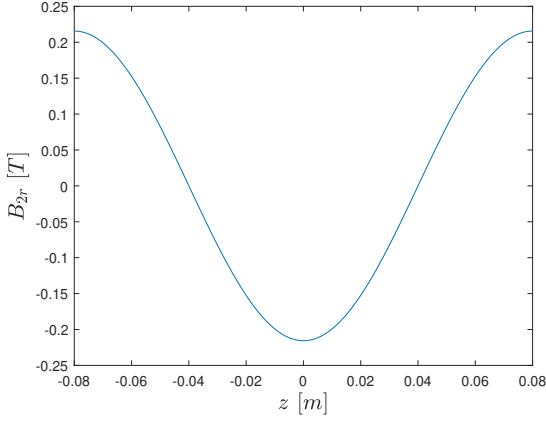


Figure 2.14: Internal axially magnetised PM array topology : Axial magnetic flux density as a function of r with $z = \tau_p/4$

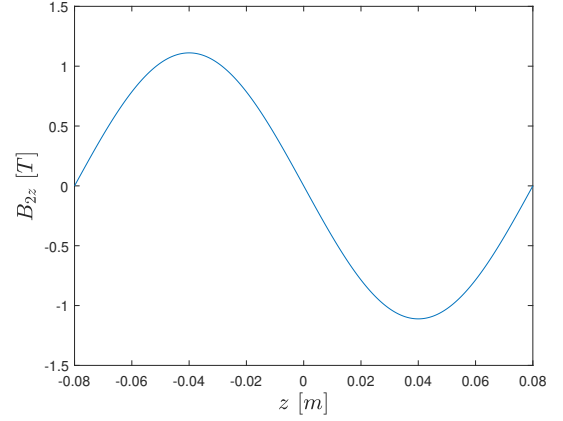
2.5.4.2 Magnetic flux density in the magnetic region

The Figure 2.15 shows the evolution of the magnetic flux density in the internal PM region with $r = (R_1 + R_2)/2$ and as a function of the axial position z . Same observations as in Subsection 2.5.2.2 can be made on the results obtained in Figure 2.15. However, one can notice that the oscillations present

in the previous topologies are not present for this topology. Indeed, a lower number of harmonics has been used to ensure sufficiently consistent results.



(a) Radial Component

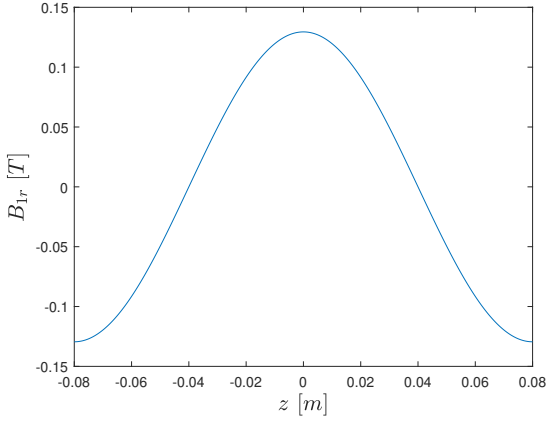


(b) Axial Component

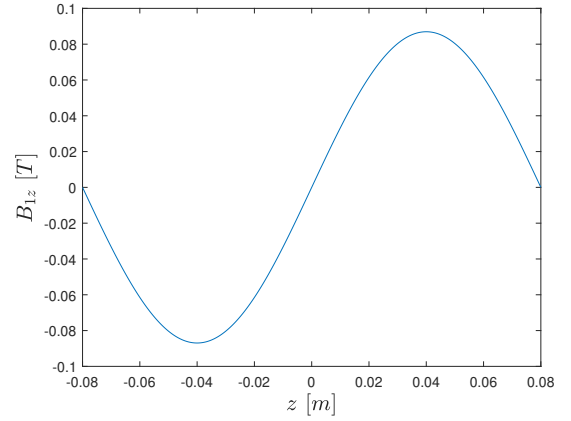
Figure 2.15: Internal PM region : Magnetic flux density as a function of z with $r = 35$ [mm]

2.5.4.3 Magnetic flux density in the air gap region

The Figure 2.16 shows the evolution of the magnetic flux density in the air gap region with $r = (R_2 + R_3)/2$ and as a function of the axial position z . Same observations as in Subsection 2.5.2.3 can be made on the results obtained in Figure 2.16. Nevertheless, it is interesting to add that the radial magnetic flux density at the centre of the air gap is lower for TPMA made up of axially magnetised PMs than for TPMA composed of dual Halbach array.



(a) Radial Component



(b) Axial Component

Figure 2.16: Air gap region : Magnetic flux density as a function of z with $r = 75$ [mm]

Chapter 3

Modeling of Force Output

The objective of this chapter is to establish an analytical model that allows the calculation of the force output. In this study, the force output is called the thrust. The analytical model of the thrust is based on the analytical models of the magnetic fields that has been described in the previous sections. Several thrust models are developed depending on the type of windings used. These windings can support either single-phase, double-phase or three-phase current. A model is established for each of these cases.

One of the main purposes of this section is to establish the relationship between the current through the coils and the thrust produced by the TPMA. In the context of the use of TPMAs as an active suspension, knowledge of this relationship is very important. Indeed, according to inverse dynamics of an actuator, the desired thrust produced by the actuator is calculated according to the dynamic constraints imposed on it. Thus, by using the thrust model, it is possible to calculate the input current to be injected. It is also preferable to obtain a linear relationship between the current and the thrust in order to simplify the real time control of the actuator or in this case the active suspension [21].

To calculate the force produced by electromagnetic products, three methods are possible: coenergy method, Maxwell stress tensor method and Lorentz force law [2]. The latter is particularly suitable for calculating the thrust of the TPMA. Indeed, it allows to calculate directly the thrust produced by the energized windings in an external magnetic field. The Lorentz force law states that a segment $d\mathbf{l}$ traversed by a current \mathbf{I}_w , immersed in an external magnetic field \mathbf{B} , undergoes a Force equal to

$$d\mathbf{F} = I_w d\mathbf{l} \times \mathbf{B} \quad (3.1)$$

This equation allows us to deduce the total thrust force produced by the TPMA with different winding configurations. In the remainder of this chapter the calculated forces are expressed by pole pitch so that the total length of the TPMA is not taken into account. As can be seen in the Equation 3.1, the magnetic field directly influences the thrust produced, so the topology of the TPMA directly influences it. It is therefore preferable to use a topology that maximises the magnetic field in the winding region and therefore in the air gap. This is the main reason why the rest of the study in this work focuses only on the dual Halbach array topology.

3.1 Assumptions

Firstly, before starting the analytical model, it is necessary to make certain assumptions. These assumptions aim to facilitate the mathematical development without losing too much precision on the results obtained. Three assumptions are made

1. Eddy currents in the stator and mover are neglected.
2. As in the previous chapter, the permeability of the iron parts is considered infinite. Thus the effects of saturation and hysteresis are negligible.
3. The armature is slotless
4. The length of the TPMA is considered infinite.

A slotless armature will reduce the maximum thrust that can be developed by the TPMA but the ripple force will also be reduced. This type of fitting is preferable to limit the variations of the thrust and thus obtain a smooth dynamic for the actuator.

A infinite length made greatly facilitates the analytical model but neglects edge effects. These edge effects are one of the main causes of thrust fluctuation. Thus the analytical model developed in this chapter tends to minimise the calculated ripple force.

3.2 Thrust for Single-Phase Winding Pattern

The thrust force is dictated by Lorentz's law described in Equation 3.1. This equation can be rewritten in its integral form

$$F = \int_V (J \times B) dV \quad (3.2)$$

where J is the current density and V is the volume of the air gap between the two arrays of Halbach magnets. Given the presence of the vector product between the magnetic flux density and the current density, only the radial component of B produces thrust. The structure of the dual Halbach array TPMA for a single phase is shown in Figure 3.1. Each of the windings occupies a width of τ_w and two coils of a phase are separated by a distance τ_{wp} which is the winding pitch. The choice of these dimensions is explained in the following.

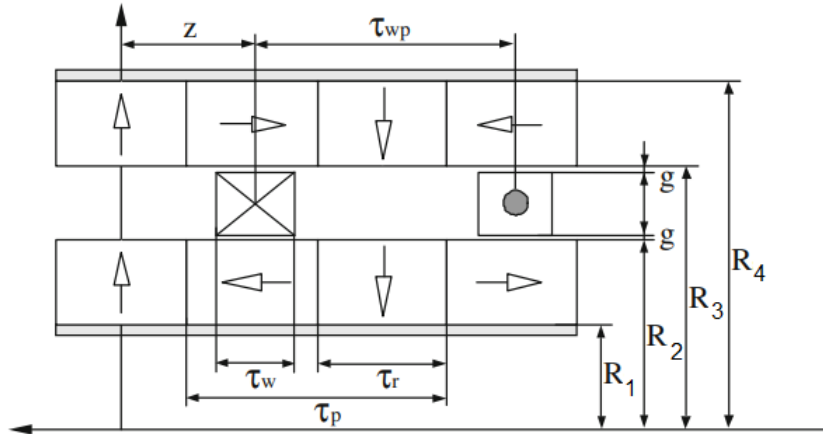


Figure 3.1: Structure of the TPMA with single-phase windings [2]

Combining the two Equations 3.2 and 2.40, the thrust force exerted on one coil is given by [22]

$$F_w = -4\pi J \sum_{n=1}^{\infty} K_{rn} \sin\left(m_n \frac{\tau_w}{2}\right) \cos(m_n z) \quad (3.3)$$

with

$$K_{rn} = \int_{R_a}^{R_i} r [a_{1n} I_1(m_n r) + b_{1n} K_1(m_n r)] dr \quad (3.4)$$

where $R_a = R_2 + g$ (g is the air gap between the armature and the PM arrays) which is the internal radius of the armature and $R_i = R_3 - g$ the external radius. The force exerted on the winding is obtained by using the result of Equation 3.3

$$\begin{aligned} F_{wp} &= F_w(z) - F_w(z - \tau_{wp}) \\ &= 8\pi J \sum_{n=1}^{\infty} K_n \sin\left[m_n \left(z - \frac{\tau_{wp}}{2}\right)\right] \end{aligned} \quad (3.5)$$

with

$$K_n = \sin\left(m_n \frac{\tau_w}{2}\right) \sin\left(m_n \frac{\tau_{wp}}{2}\right) K_{rn} \quad (3.6)$$

It is preferable to express the relationship established in Equation 3.5 as a function of J_{rms} which is the root mean square of the current density. J_{rms} is given by

$$J = \sqrt{2} J_{rms} \cos \omega t \quad (3.7)$$

Combining Equations 3.7 and 3.5 gives the expression

$$F_{wp} = -8\sqrt{2}\pi J_{rms} \sum_{n=1}^{\infty} K_n \sin\left(m_n \left(z - \frac{\tau_{wp}}{2}\right)\right) \cos \omega t \quad (3.8)$$

Then it is possible to express the relationship between the movement of the armature with respect to the stator. In this case, the armature moves in synchronism with the AC frequency [2]. Thus with v being the speed of the mover and z its relative position, the relationship of synchronous movement between the armature and the current frequency is given by

$$\omega t = \frac{\pi v}{\tau_p} t = \frac{\pi}{\tau_p} z \quad (3.9)$$

Finally, in order to increase the thrust produced, it is preferable to have the distance between two coils of the same phase equal to the pole pitch of the PMs. This allows the whole winding to be used to produce force. So the expression of the force produced for a single phase winding and for a single pole pitch is given by

$$F_{wp} = -8\sqrt{2}\pi J_{rms} \sum_{n=1}^{\infty} K_{rn} \cos(m_n z) \cos\left(\frac{\pi z}{\tau_p}\right) \quad (3.10)$$

By applying the relationship established in Equation 3.10, it is possible to obtain the variation of the thrust as a function of the relative position of the mover z . This variation is illustrated in Figure 3.2 for a dual Halbach array TPMA with the dimensions described in Table 2.1 and for $J_{rms} = 1.5 \times 10^6 [A/m^2]$. The maximum force peaks are reached when the winding is aligned with the centre of the radially magnetised PMs. Minima are reached when the winding is centred with the axially magnetised PMs. The period of variation of the thrust is therefore equal to the pole pitch of the PMs.

An important remark is that the fundamental force, which is defined as the constant part of the thrust, is zero in the case of a single-phase winding which is really not desirable for the actuator to have good dynamics [22].

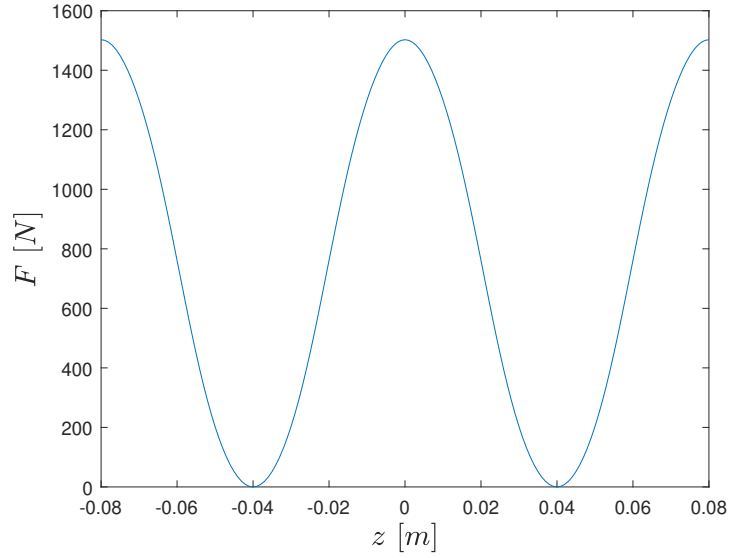


Figure 3.2: Thrust generated by single-phase winding TPMA

3.3 Thrust for Double-Phase Winding Pattern

The structure of a TPMA with double-phase windings is shown in Figure 3.3. In this study, the width of the windings is considered to be the same for each phase.

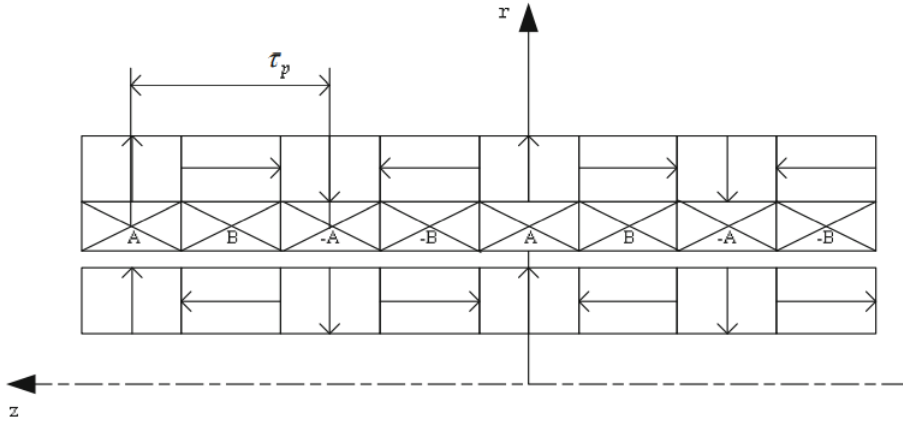


Figure 3.3: Structure of a TPMA with double-phase windings [2]

The neighbouring windings have current density with opposite phase. The input current densities in phases A and B are

$$J_A = \sqrt{2}J_{rms} \cos wt \quad (3.11)$$

$$J_B = \sqrt{2}J_{rms} \sin wt \quad (3.12)$$

Thus the thrusts generated by each of the phases are given by

$$F_A = 8\sqrt{2}\pi J_{rms} \left(\sum_{n=1}^{\infty} K_n \sin m_n \left(z - \frac{\tau_p}{2} \right) \cos \frac{\pi z}{\tau_p} \right) \quad (3.13)$$

$$F_B = 8\sqrt{2}\pi J_{rms} \left(\sum_{n=1}^{\infty} K_n \sin m_n (z - \tau_p) \sin \frac{\pi z}{\tau_p} \right) \quad (3.14)$$

It can therefore be seen that the two forces do not cancel out simultaneously for the same axial position z . This allows the TPMA to produce thrust continuously, which was not the case for a single phase TPMA.

The total thrust is obtained by adding the thrust of each of the phases

$$\begin{aligned} F &= F_A + F_B \\ &= F_1 + F_r \\ &= F_1 + \sum_{n=2}^{\infty} F_n \cos \left[(2n-1 + (-1)^n) \frac{\pi z}{\tau_p} \right] \end{aligned} \quad (3.15)$$

where F_1 is the fundamental force that causes the constant thrust throughout the different mover positions, F_r is the force ripple that causes the fluctuations of the thrust and F_n which is the magnitude of the force ripple created by the $(2n-1)^{\text{th}}$ harmonic component [2]. The expressions for these forces are given by

$$F_1 = -8\sqrt{2}\pi J_{rms} K_1 \quad (3.16)$$

$$F_n = (-1)^n 8\sqrt{2}\pi J_{rms} K_n \quad (3.17)$$

and the maximum of the force ripple is given by

$$F_{rm} = 8\sqrt{2}\pi J_{rms} \sqrt{\sum_{n=2k}^{\infty} (K_n - K_{n+1})^2} \quad (3.18)$$

The expression given in the Equation 3.15 indicates that the ripple force is a disturbance which is a periodic function of the position of the translator relative to the stator. It should also be noted that the ripple force is an electromagnetic effect that only occurs when the input current is non-zero. One of the objectives of good TPMA design is to minimise this ripple force, which reduces the dynamic performance of the actuator [7].

By applying the relationship established in Equation 3.15, it is possible to obtain the variation of the thrust as a function of the relative position of the mover z . This variation is illustrated in Figure 3.4 for a dual Halbach array TPMA with the dimensions described in Table 2.1 and for $J_{rms} = 1.5 \times 10^6$ [A/m²]

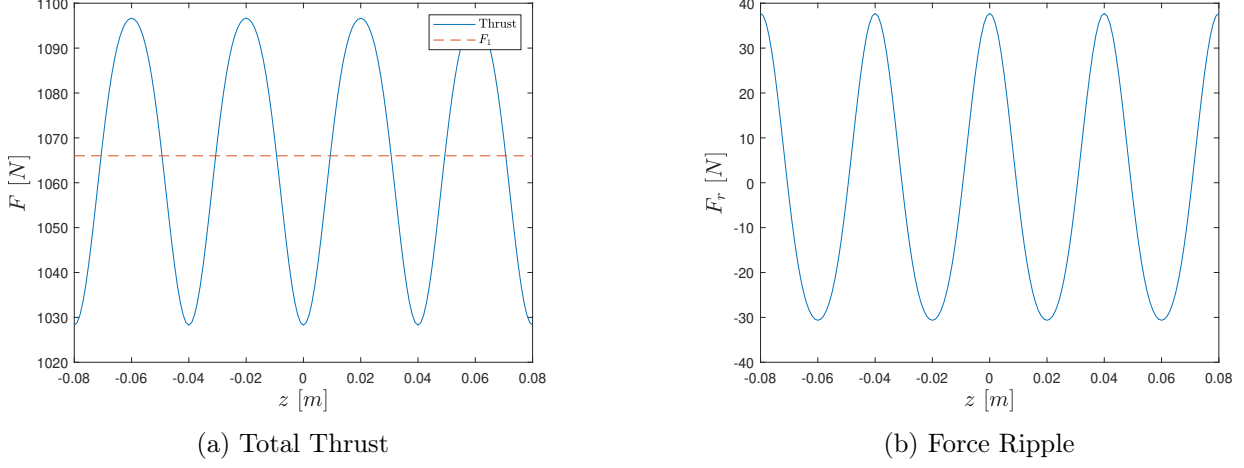


Figure 3.4: Thrust variation generated by double-phase winding TPMA

As shown in Figure 3.4 and similar to the single phase winding, the maximums are reached when the winding is aligned with the radially magnetised PMs. This is the expected result as the maximum value of the radial component of the magnetic field is reached at this position. Since the distance between two coils is half the pole pitch of the PMs, the period of variation of the thrust is $\tau_p/2$.

Compared to single-phase winding, there is the presence of the fundamental force. This fundamental force is worth 1066 [N] and ensures that the TPMA can provide continuous thrust. The variation of the thrust is obtained, as described by Equation 3.15, by adding to this fundamental force the ripple force.

Compared to the single-phase winding, the thrust maxima are lower but the thrust only varies in a range of about 70 [N] since the ripple force is much lower. The dual-phase winding also allows for continuous delivery of thrust, which is not the case for the single-phase winding.

3.4 Thrust for Three-Phase Winding Pattern

The structure of a TPMA with three-phase windings is shown in Figure 3.5. In this study, the width of the windings is considered to be the same for each phase and is equal to $\tau_w = \tau_{wp}/3 = \tau_p/3$.

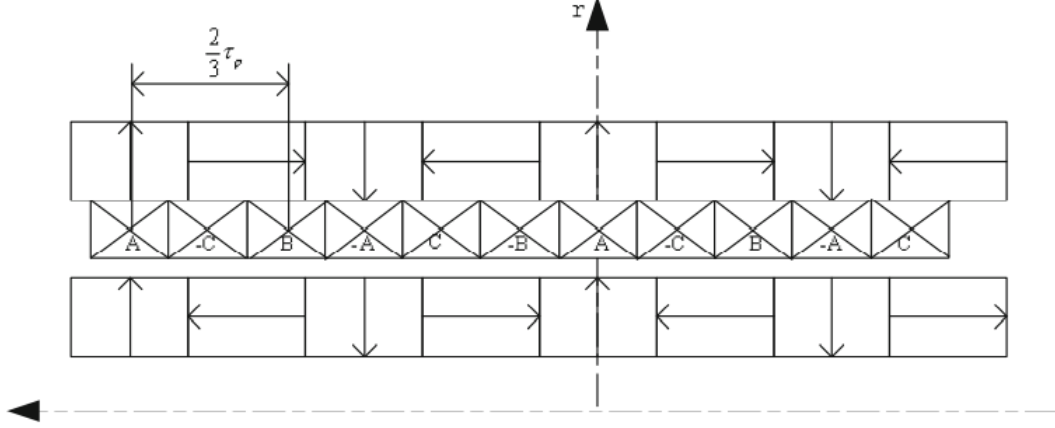


Figure 3.5: Structure of a TPMA with three-phase windings [2]

In the case of a TPMA with a three-phase winding, the thrust produced is sensitive to the initial position of the mover x relative to the stator [22]. The Equation 3.9 must be rewritten taking into account x

$$\omega t = \frac{\pi v}{\tau_p} t = \frac{\pi}{\tau_p} (z - x) \quad (3.19)$$

Thus the thrust produced by a single phase winding is given by

$$F_{wp} = -8\sqrt{2}\pi J_{rms} \sum_{n=1}^{\infty} K_n \sin \left(m_n \left(z - \frac{\tau_{wp}}{2} \right) \right) \cos \left[\frac{\pi}{\tau_p} (z - x) \right] \quad (3.20)$$

and it can be seen that the thrust no longer depends solely on the instantaneous position of the mover but also on its initial position. Two examples of the initial position are shown in Figure 3.6, a study on the best starting position is developed later.

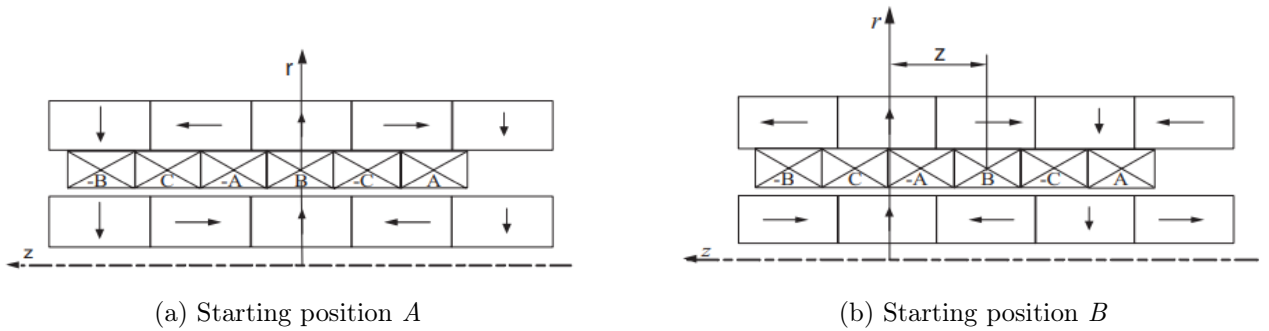


Figure 3.6: Two different starting positions

The current density between the three phases is out of phase by 120° , so the current densities are given by

$$\begin{aligned} J_A &= \sqrt{2}J_{rms} \cos\left(\omega t + \frac{2}{3}\pi\right) \\ J_B &= \sqrt{2}J_{rms} \cos\omega t \\ J_C &= \sqrt{2}J_{rms} \cos\left(\omega t - \frac{2}{3}\pi\right) \end{aligned} \quad (3.21)$$

By injecting the results of Equation 3.21 into the thrust expression of Equation 3.20, the expression of the thrust produced by each phase is obtained

$$F_A = -8\sqrt{2}\pi J_{rms} \sum_{n=1}^{\infty} K_n \sin\left(m_n \left(z + \frac{2}{3}\tau_p - \frac{\tau_p}{2}\right)\right) \cos\left(\frac{\pi(z-x)}{\tau_p} + \frac{2\pi}{3}\right) \quad (3.22)$$

$$F_B = -8\sqrt{2}\pi J_{rms} \sum_{n=1}^{\infty} K_n \sin\left(m_n \left(z - \frac{\tau_p}{2}\right)\right) \cos\left(\frac{\pi(z-x)}{\tau_p}\right) \quad (3.23)$$

$$F_C = -8\sqrt{2}\pi J_{rms} \sum_{n=1}^{\infty} K_n \sin\left(m_n \left(z - \frac{2}{3}\tau_p - \frac{\tau_p}{2}\right)\right) \cos\left(\frac{\pi(z-x)}{\tau_p} - \frac{2\pi}{3}\right) \quad (3.24)$$

It remains to add these three forces to obtain the total thrust produced by the TPMA

$$\begin{aligned} F &= F_A + F_B + F_C \\ &= F_1 + \sum_{n=3k}^{\infty} F_{n0} \cos\left(\frac{2n\pi z}{\tau_p} - \frac{\pi x}{\tau_p}\right) + \sum_{n=3k+1}^{\infty} F_{n1} \cos\left(\frac{(2n-2)\pi z}{\tau_p} + \frac{\pi x}{\tau_p}\right) \end{aligned} \quad (3.25)$$

In this case, the fundamental force is directly affected by the initial position of the mover:

$$F_1 = 12\sqrt{2}\pi J_{rms} K_1 \cos\left(\frac{\pi x}{\tau_p}\right) \quad (3.26)$$

while the ripple force is also dependent on it and on the instantaneous position. In the case of a three-phase winding, the ripple force is composed of two terms

$$\begin{aligned} F_{n0} &= (-1)^k 12\sqrt{2}\pi J_{rms} K_n \\ F_{n1} &= (-1)^{k+1} 12\sqrt{2}\pi J_{rms} K_n \end{aligned}$$

First, it is necessary to determine the best initial position of the mover as this is a parameter that can be directly controlled. The variation of the fundamental force as a function of the initial position of the mover x is shown in Figure 3.7. It can be directly observed that x must be equal to a multiple of the pole pitch. This means that the phase must be aligned with a radially magnetized PMs, as shown in Figure 3.6a. This starting position is maintained in the following results.

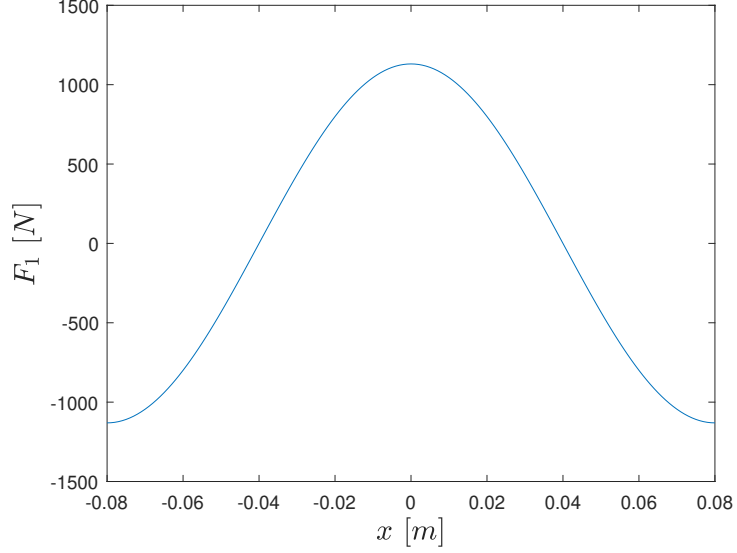
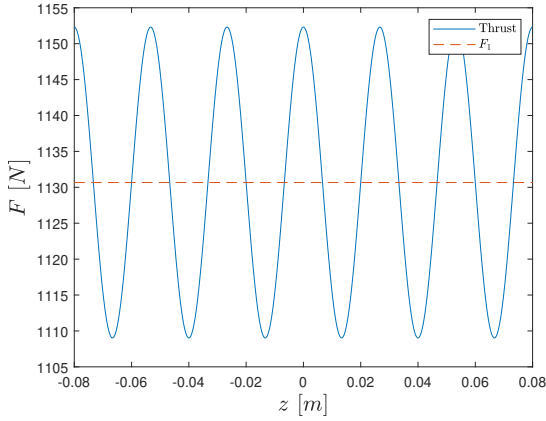
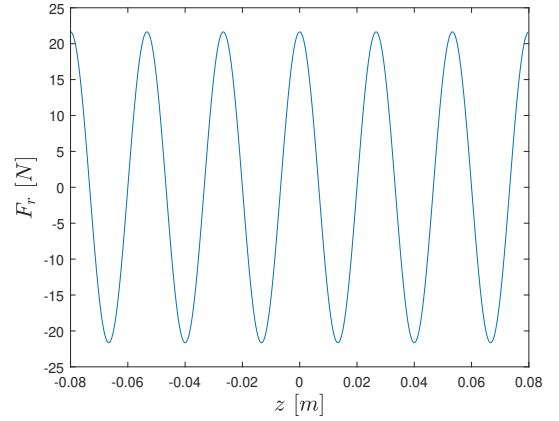


Figure 3.7: Fundamental force as a function of the starting position x

By applying the relationship established in Equation 3.25, it is possible to obtain the variation of the thrust as a function of the relative position of the mover z . This variation is illustrated in Figure 3.8 for a dual Halbach array TPMA with the dimensions described in Table 2.1 and for $J_{rms} = 1.5 \times 10^6$ [A/m²]



(a) Total Thrust



(b) Force Ripple

Figure 3.8: Thrust variation generated by three-phase winding TPMA

As shown in Figure 3.8 and similar to the single and double phase winding, the maximums are reached when the winding is aligned with the radially magnetized PMs. Since the distance between two coils is a third of the pole pitch of the PMs, the period of variation of the thrust is $\tau_p/3$.

3.5 Conclusion

The results of the different types of winding are shown in the Table 3.1. It can be seen that the TPMA can develop its maximum thrust when the winding is single-phase. However, with a single-phase winding the force varies enormously until it is cancelled out in certain positions. The single-phase winding is therefore not viable if the objective is to have smooth dynamics.

If you compare three-phase and two-phase, the result is clear. Three-phase has a better fundamental force and a lower ripple force than two-phase. Thus three-phase is the best choice among those studied.

	F_{\max} [N]	F_1 [N]	$F_{r,\max}$ [N]
Single-phase	1502.61	0	1502.61
Double-phase	1096.65	1066	37.73
Three-phase	1152.31	1130.67	21.64

Table 3.1: Results obtained for the different types of winding

Chapter 4

Optimisation of the design

In the previous chapters, the objective was to select the optimal topology and winding type. The result obtained is that the dual Halbach array topology with a three-phase current seems to be the ideal candidate to obtain the best possible performance. However, the dimensions of this TPMA have yet to be determined.

The objective of this chapter is to find the optimal dimensions of the TPMA to obtain the best possible performance under certain constraints. In this study, the constraints are mainly space constraints, no performance constraints have been stated.

In the first instance, the objective of the optimisation is to maximise the thrust force within the space constraints for the TPMA. This problem is solved using the PSO method.

Then, the optimisation is done on two objectives. The first is still to maximise thrust and the second is to minimise ripple force. This MOO is carried out by the mathematical method that was retained by the Single-Objective Optimisation (SOO).

Finally, the final design is presented and its performance is compared with the results of the baseline design that was studied in the previous chapters.

4.1 SOO problem

4.1.1 Definition and Mathematical formulation of the problem

Initially, the optimisation problem has only one objective, to maximise the constant thrust or fundamental thrust F_1 produced by the TPMA. Thus $f(x) = F_1(x)$ is the function to be maximised. This function depends on the vector of variables in x . This vector consists of the variables of the problem which are the radii R_1 , R_2 , R_3 and R_4 as well as the width of the pole pitch τ_p . Initially, the ratio of radial and axial magnets remains constant and is 1. This first optimisation allows us to understand the trend of the dimensions taken by the variables of the problem to maximise $f(x)$.

Then, it remains to define the constraints on these five variables. The constraints imposed on the outer radius of the external PMs come from the maximum space requirement that the TPMA can take. This value is taken from [4] which uses the TPMA in the suspension system of a high speed train. The constraint on the inner radius of the inner PMs is taken in order to leave enough room for the yoke that is inserted within the TPMA. The constraint on the width of the pole pitch is taken in order to

have enough magnet pole repetition over the entire length of the TPMA which is about 1 [m] in the case studied in [4]. The constraints g_i are given by

$$R_1 \geq 20 \text{ [mm]} \quad (4.1)$$

$$R_2 \geq R_1 \quad (4.2)$$

$$R_3 \geq R_2 \quad (4.3)$$

$$R_4 \geq R_3 \quad (4.4)$$

$$R_4 \leq 100 \text{ [mm]} \quad (4.5)$$

$$\tau_p \leq 80 \text{ [mm]} \quad (4.6)$$

$$(4.7)$$

Since the problem posed is a constrained single objective optimisation problem, it has only one maximum. This maximum is sought using two algorithms which are described in the following.

4.1.2 PSO Resolution

Introduction to PSO

PSO is a population-based stochastic optimisation technique. It is largely inspired by natural facts such as bird flocking. It has many similarities with evolutionary algorithms like Genetic Algorithm (GA). As with evolutionary algorithms, a random population is generated to search for the optimum to an optimisation problem. However, in the case of PSO, no evolution operator is used [23].

The population called swarm consists of particles that each refer to a value of the given problem. In our case, each of the particles has a position vector $x_i(t)$ which is made up of possible values of the TPMA dimensions. Each particle aims to explore the space of possible solutions to the problem at hand in search of the best one. Its exploration is influenced by the other particles in the swarm, which constitutes its social behaviour, and also by its best position, which constitutes its personal experience. Thus, at each time step, a velocity vector $v_i(t)$ is defined for each particle, which directs the current position of the particle towards both the best recorded position of the swarm and the best recorded position of the particle. A vector representation of the PSO is possible and is shown in Figure 4.1

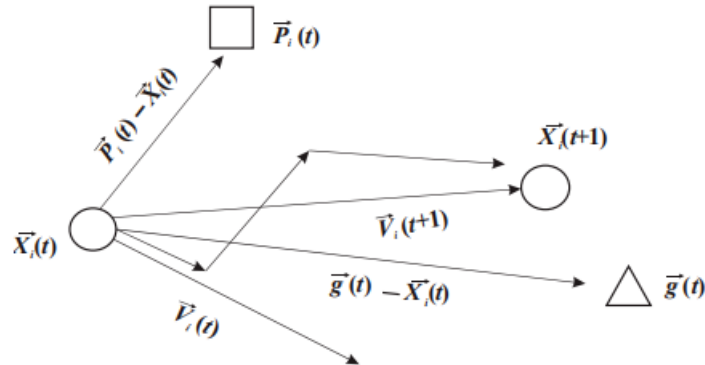


Figure 4.1: Vector representation of the PSO [24]

Operation of PSO

From the Figure 4.1, it can be seen that the new position of the particle $\vec{X}_i(t+1)$ is obtained using 3 vectors

- $\vec{V}_i(t)$ the speed of the particle at time t
- $\vec{P}_i(t)$ the best position of the particle
- $\vec{g}(t)$ the global best position of the swarm

Thus the experience of the particle and the group effect cooperate to find the optimum of the problem. Mathematically, the following relationships can be derived

$$\vec{V}_i(t+1) = \omega \vec{V}_i(t) + c_1 r_1 (\vec{P}_i(t) - \vec{X}_i(t)) + c_2 r_2 (\vec{g}(t) - \vec{X}_i(t)) \quad (4.8)$$

$$\vec{X}_i(t+1) = \vec{X}_i(t) + \vec{V}_i(t+1) \quad (4.9)$$

where

- $\omega \vec{V}_i(t)$ is the inertia term and the parameter ω is the inertia coefficient. This term quantifies the importance of the current velocity of the particle towards finding the new position.
- $c_1 r_1 (\vec{P}_i(t) - \vec{X}_i(t))$ is the cognitive component. It expresses that the particle uses its personal experience to search for a better position. The factor r_1 is a random number between 0 and 1. The parameter c_1 is an acceleration coefficient.
- $c_2 r_2 (\vec{g}(t) - \vec{X}_i(t))$ is the social component. This term expresses the group effect, the group cooperates so that each particle improves its position. The best position of the swarm $\vec{g}(t)$ is shared at each particle. The factor r_2 is a random number between 0 and 1. The parameter c_2 is an acceleration coefficient.

The inertia term corresponds to the diversification in the search procedure. While the other two terms correspond to intensification in the search procedure. A good balance between diversification and intensification allows an optimal search procedure [23].

Algorithm description

The algorithm procedure is described by the following steps [25]

- **Step 1** The swarm is randomly initialized with positions that are consistent with the constraints imposed by the problem
- **Step 2** The value of each particle is evaluated. For a given position \vec{X}_i of particle i , the value of the particle is given by $F_1(\vec{X}_i)$.
- **Step 3** The best position \vec{P}_i of the particle i is updated if its current value is better than its personal best. The same applies to the best position in the swarm. Then the velocity \vec{V} of each particle is updated using the relation in Equation 4.8.
- **Step 4** The position of each particle is updated using the relation in Equation 4.9.
- **Step 5** Return to step 2 and the algorithm is repeated until convergence or the stopping criterion is reached.

Coefficients' settings

In order to implement the algorithm, it remains to select the values of the different parameters. One of the advantages of PSO is that there are very few parameters to adjust. The values of these parameters must be chosen in order to ensure the convergence and stability of the algorithm. In [26], the search procedure of the algorithm is considered as a dynamic system since it consists of difference equations. Thus, it can be analysed by an eigenvalue analysis. It is possible to control this analysis so that the system converges and is stable. Equation 4.8 is rewritten by introducing the constriction factor K

$$\vec{V}_i(t+1) = K \left[\vec{V}_i(t) + c_1 r_1 \left(\vec{P}_i(t) - \vec{X}_i(t) \right) + c_2 r_2 \left(\vec{g}(t) - \vec{X}_i(t) \right) \right] \quad (4.10)$$

The eigenvalue analysis gives an expression for the constriction factor in Equation 4.11 that ensures the convergence and stability of the algorithm.

$$K = \frac{2}{\left| 2 - \varphi - \sqrt{\varphi^2 - 4\varphi} \right|} \quad \text{with} \quad \varphi = c_1 + c_2 \quad (4.11)$$

The convergence of the system is entirely controlled by the value of φ . The value of φ must be greater than 4 in order to ensure the stability of the algorithm. However, it should be taken into account that increasing the value of φ decreases the value of K and thus reduces the diversification. The algorithm then takes longer to converge. The values usually taken are as follows $c_1 = c_2 = 2.05$, $\varphi = 4.1$ so $K = 0.729$ [27].

Since the coefficient of inertia ω has been replaced by the constriction factor K , it is necessary to define a range of maximum and minimum velocities in order to avoid excessively large steps occurring during the first iterations of the algorithm [27]. By good practice, these speeds are defined by

$$V_i(t) \in [-V_{max}, V_{max}] \quad \text{with} \quad V_{max} = 0.5(X_{max} - X_{min})$$

In [28], It is suggested that the population size be chosen as twice the number of variables in the problem. Thus the population size is $N = 2 \times 5 = 10$.

The number of iterations should be chosen to allow the algorithm to converge to the optimum. In this case, 100 iterations are sufficient.

Analysis of results

The maximum fundamental thrust obtained during the iterations is shown in Figure 4.2. Convergence is reached after approximately twenty iterations. The maximum fundamental thrust obtained is 1371.47 [N]. The dimensions of this maximisation are shown in the Table 4.1.

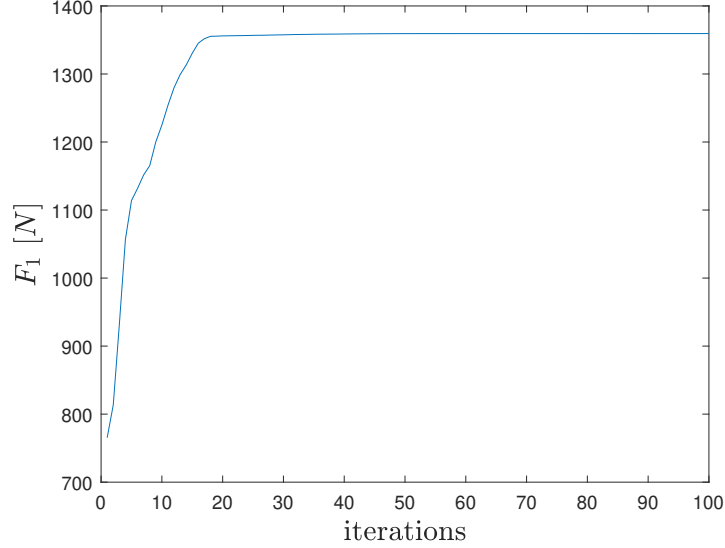


Figure 4.2: Convergence of the thrust

Geometric Parameters	Value
Inner radius of internal PMs, R_1	20 [mm]
Outer radius of internal PMs, R_2	65.0464 [mm]
Inner radius of external PMs, R_3	92.2655 [mm]
Outer radius of external PMs, R_4	100 [mm]
Pole pitch, τ_p	80 [mm]

Table 4.1: Dimensions of the dual Halbach array TPMA obtained after PSO

The curve of the magnetic flux density in the middle of the air gap is shown in Figure 4.3. It can be seen that compared to the magnetic flux density shown in Figure 2.8a for the standard dimensions of the Table 2.1, the peak reached by the curve has approximately doubled with the optimised dimensions. This increase was expected as the magnet volume increased significantly with the optimised dimensions. Especially in the internal PMs, which are crossed by more magnetic flux density lines. This has a direct impact on the thrust produced, which is considerably increased.

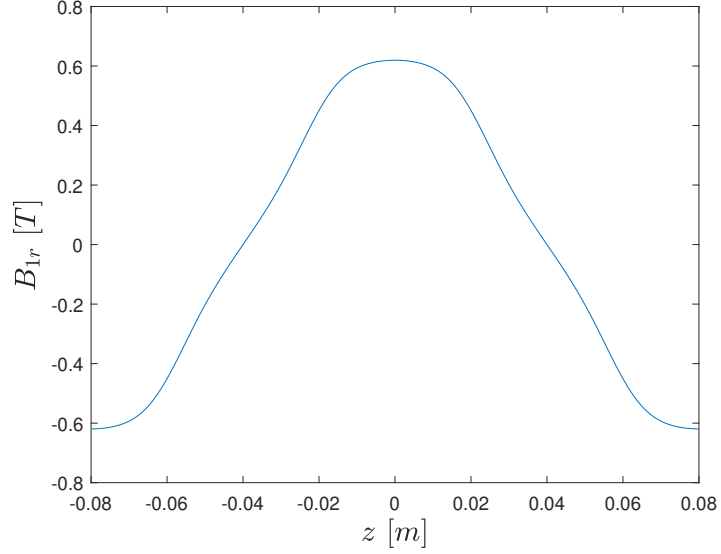
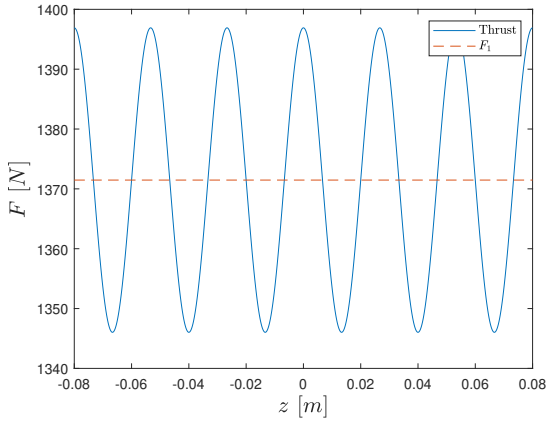
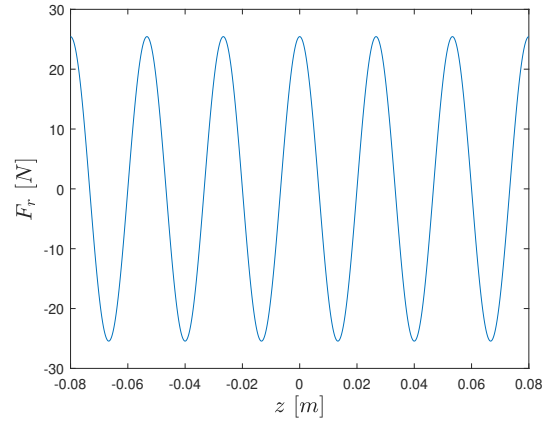


Figure 4.3: Radial magnetic flux density as a function of z with $r = 78.65595$ [mm]

The graph of the thrust is shown in Figure 4.4. The peaks reached by the thrust is obviously higher than those reached by the standard dimensions. However, it can also be noted that the ripple force it has increased slightly. However, the relative ripple force has decreased as the fundamental force has increased.



(a) Total Thrust



(b) Force Ripple

Figure 4.4: Thrust variation generated by a TPMA with PSO dimensions

In view of the results obtained, it can be concluded that the optimisation by PSO to maximise the thrust produced by the TPMA is convincing. The fundamental thrust increased by 21.29%, from 1130.67 [N] with the standard dimensions to 1371.47 [N] with the optimised dimensions. The algorithm is relatively easy to implement and few parameters have to be set. However, the computation time is not negligible even though the problem does not have many variables to optimise.

4.2 MOO problem

4.2.1 Definition and Mathematical formulation of the problem

The objective of the Section 4.1 was to verify the tendency of the geometric variables of the problem to maximise the thrust of the TPMA. It was observed that the inner radius of the inner magnets R_1 and the outer radius of the outer PMs R_4 take the value of their respective bounds in order to increase the volume of the PMs. The pole pitch of the PMs τ_p does the same and for the same reason. Thus, in the rest of the study, these variables are fixed at their respective bound values. They are no longer variables of the optimisation problem.

The outer radius of the inner PMs and the inner radius of the outer PMs remain variables in the problem. The proportion $\alpha = \tau_r/\tau_p$ of radially magnetised PMs in the pole pitch becomes a new variable in the problem. This ratio is used to show the impact that the magnetisation vector \mathbf{M} has on the performance of the TPMA.

In the Section 4.1, only the objective of maximising thrust is taken into account. However, in order for the TPMA to perform well, the ripple force of this thrust must be as low as possible. Thus the optimisation problem becomes a MOO whose two objectives are the maximisation of thrust and the minimisation of ripple force. The new optimisation problem is then defined with a vector of variables x that respect the constraints g_i

$$x = (R_2, R_3, \alpha)^T \quad (4.12)$$

$$R_2 > 20 \text{ [mm]} \quad (4.13)$$

$$R_3 < 100 \text{ [mm]} \quad (4.14)$$

$$\alpha \leq 1 \quad (4.15)$$

and which optimise the vector of functions $\mathbf{f}(x) = \{F_1(x), F_r(x)\}^T$

Since there are two objective functions to be optimised, they are in conflict with each other. Thus there is no single optimal solution to the problem and it is impossible (in most cases) to find for all objective functions the global optimum point of the problem. It is necessary to introduce the concept of Pareto optimality which states that a solution x of the problem is Pareto optimal if and only if there is no other solution which dominates it. In MOO problem, dominance determines the goodness of a solution. Thus a solution x_1 dominates a solution x_2 if x_1 is not worse than x_2 in all objectives or if x_1 is strictly better than x_2 in at least one objective [29].

These solutions then form a set of optimal trade-offs or a front of solutions called the Pareto front [28]. The objective of this section is then to find one of these solutions while respecting the constraints of the problem.

4.2.2 VEPSO Resolution

Introduction to VEPSO

Vector evaluated PSO or VEPSO is one form of PSO adapted for MOO problems. Its design is simple and derives directly from the description of the PSO. However, in this case, two objective functions need to be optimised. Thus each objective function is assigned to a swarm which searches for its optimum.

Nevertheless, the two swarms will exchange information in order to influence each other. Since there are only two objective functions to be optimised, the exchange of information does not need to be complex.

Operation of VEPSO

Let us assume that the first swarm is associated with thrust and the second swarm is associated with ripple force. Thus, the best position of the second swarm $g_2(t)$, which corresponds to the best reduction of the ripple force at time t , is used to determine the new velocity of the particles of the first swarm. The iteration scheme of the swarm associated with the thrust is defined by [28]

$$V_i^{[1]}(t+1) = \omega^{[1]}V_i^{[1]}(t) + c_1^{[1]}r_1 \left(P_i^{[1]}(t) - X_i^{[1]}(t) \right) + c_2^{[1]}r_2 \left(g^{[2]}(t) - X_i^{[1]}(t) \right) \quad (4.16)$$

$$X_i^{[1]}(t+1) = X_i^{[1]}(t) + V_i^{[1]}(t+1) \quad (4.17)$$

and for the swarm associated with the force ripple

$$V_i^{[2]}(t+1) = \omega^{[2]}V_i^{[2]}(t) + c_1^{[2]}r_1 \left(P_i^{[2]}(t) - X_i^{[2]}(t) \right) + c_2^{[2]}r_2 \left(g^{[1]}(t) - X_i^{[2]}(t) \right) \quad (4.18)$$

$$X_i^{[2]}(t+1) = X_i^{[2]}(t) + V_i^{[2]}(t+1) \quad (4.19)$$

The procedural steps of the algorithm are identical to those used for conventional PSO except that these steps are applied in parallel to two separate swarms.

Coefficients' settings

The choice of parameters is different from that made for the PSO. Indeed, the particles converge less quickly to an optimal solution as they are influenced by the best position of another swarm. It is therefore necessary to evolve the coefficient of inertia ω so that when the particles are close to one of the optimals, they converge more quickly. The inertia coefficient is then dynamically adjusted throughout the iterations as follows

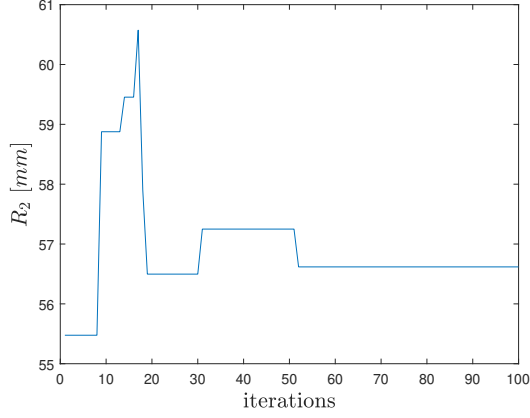
$$\omega = \omega_{\max} - [\{(\omega_{\max} - \omega_{\min}) / \text{it}_{\max}\} * \text{it}] \quad (4.20)$$

In [28] the recommended values are $\omega_{\max} = 1$, $\omega_{\min} = 0.4$ and $c_1 = c_2 = 0.2$.

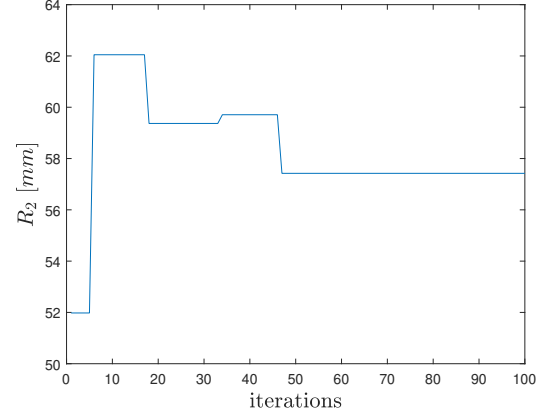
The size of the population and the number of stages are chosen in the same way as for conventional PSO: $N = 2 \times 3 = 6$

Analysis of results

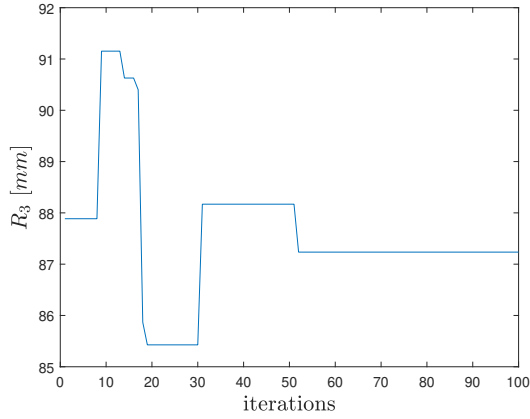
Since the algorithm is run on two swarms simultaneously, it is important to check that they converge to the same position. The convergence of each of the variables are illustrated in Figure 4.5. It can be seen that the two swarms are converging to the same position and in a fairly accurate manner.



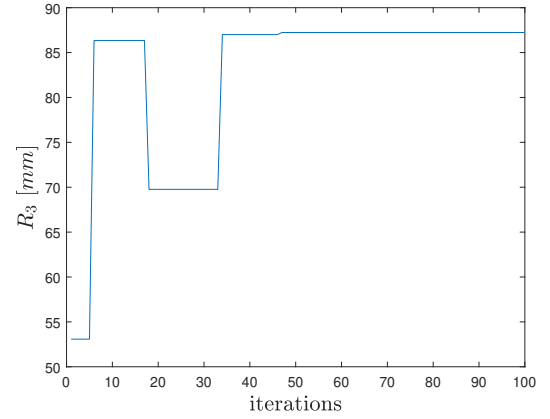
(a) Swarm 1: External radius of the internal PMs



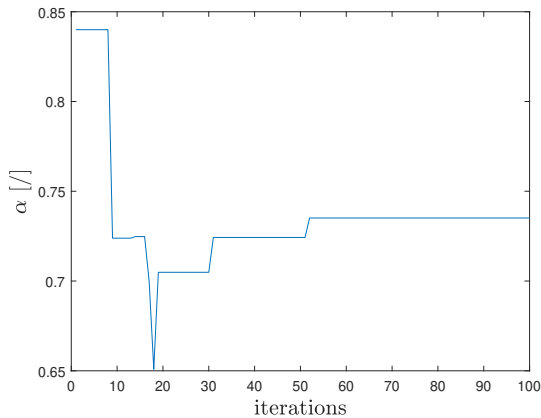
(b) Swarm 2: External radius of the internal PMs



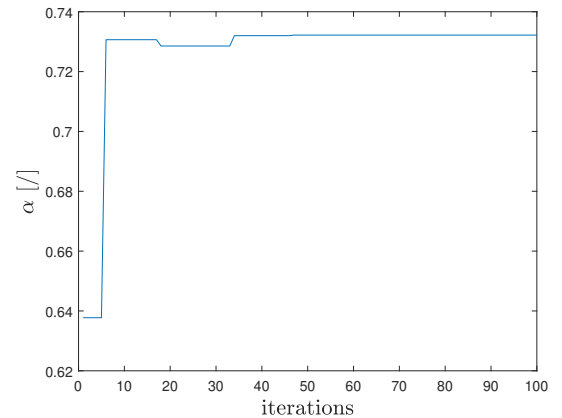
(c) Swarm 1: Internal radius of the external PMs



(d) Swarm 2: Internal radius of the external PMs



(e) Swarm 1: ratio of radially magnetised PMs



(f) Swarm 2: ratio of radially magnetised PMs

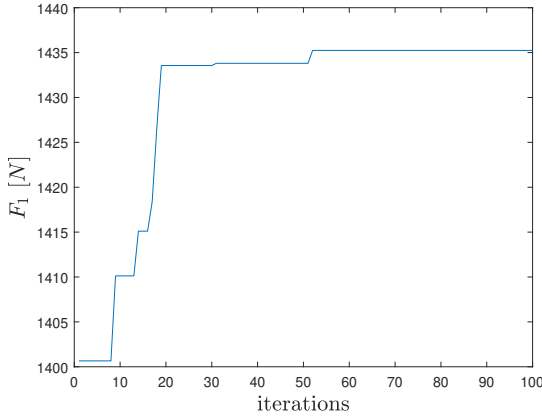
Figure 4.5: Convergence of the problem variables during the iterations

The dimensions obtained for each of the swarms are shown in the Table 4.2 where the first swarm aimed to maximise the thrust and the second one to minimise the ripple force.

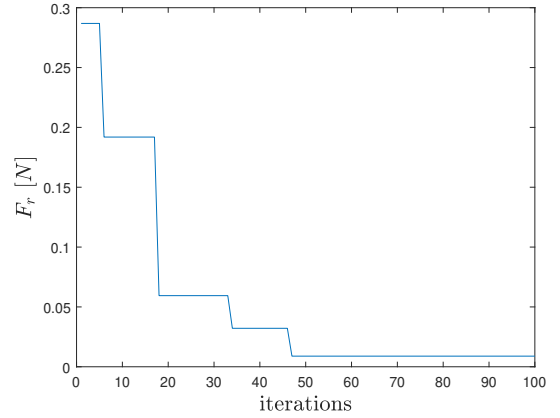
	R_2 [mm]	R_3 [mm]	α [°]
Swarm 1	56.6179	87.2349	0.735113
Swarm 2	57.4229	87.2358	0.732194
Relative difference [%]	1.4019	0.0011	0.3987

Table 4.2: Dimensions of the dual Halbach array TPMA obtained after VEPSO

As the dimensions converged to the same values, the results obtained can be considered. The convergence of the thrust and ripple force over the iterations is shown in Figure 4.6. The fundamental thrust converged around the fiftieth iteration at a value of 1435.241 [N]. The ripple force converged a little before the fiftieth iteration at the value of 0.0088775 [N]. Through these two values, we can see the impact that the α ratio has. It allowed to obtain a fundamental thrust superior to the one obtained after the PSO. It also allowed to almost cancel the ripple force.



(a) Fundamental Thrust



(b) Force Ripple

Figure 4.6: Convergence of the objective functions

However, several remarks should be made concerning the reduction of the ripple force. The first is that since edge effects are not taken into account in the analytical model, it is indeed possible to reduce the ripple force to almost zero. Unfortunately such a low value would not be achievable with these effects taken into account. The second is that the ripple force is very sensitive to changes in dimensions. The dimensions obtained are accurate to a thousandth of a millimetre, which is difficult to achieve in manufacturing. Therefore, such a reduction of the ripple force remains very theoretical.

As the fundamental force is less sensitive than the ripple force to dimensional variations, the final design conserves the dimensions obtained by the swarm 2. The variation of the magnetic field at the centre of the air for such dimensions is shown in Figure 4.7. The peak reached by the curve is lower than the one in Figure 4.3 which is obtained by PSO. However, in the Figure 4.7 it can be seen that a high magnetic flux density is maintained over a longer axial distance than in Figure 4.3. This is largely due to the increased proportion of radial magnets in the pole pitch. This will result in a higher fundamental thrust.

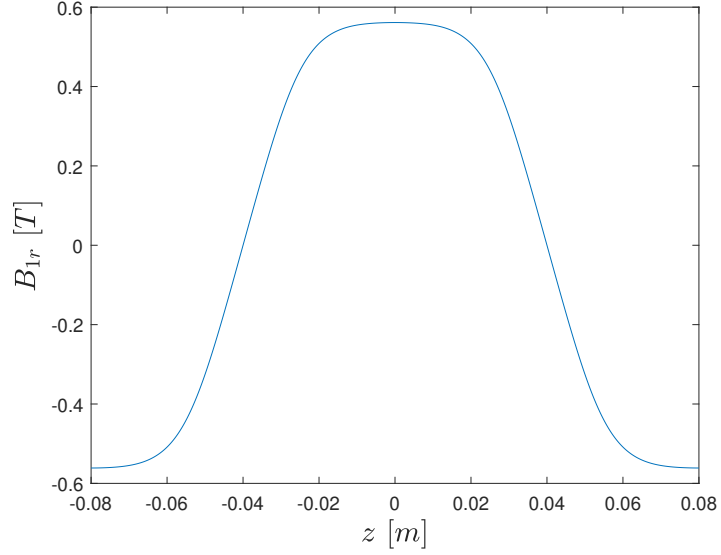
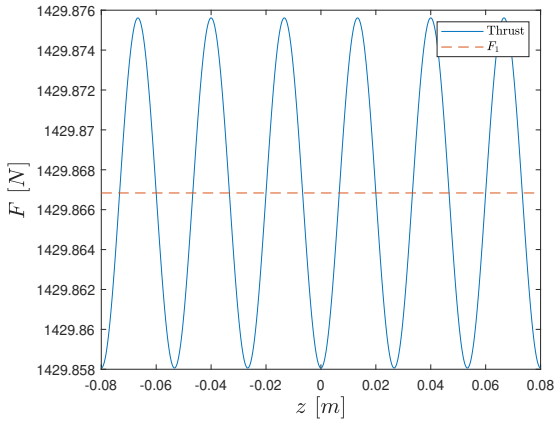
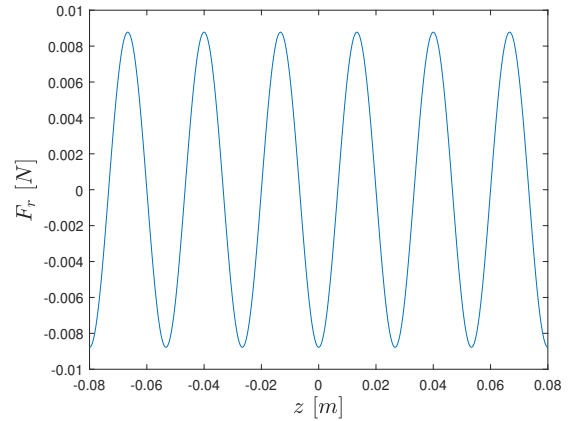


Figure 4.7: Radial magnetic flux density as a function of z with $r = 72.32935$ [mm]

The graph of the thrust is shown in Figure 4.8. The double optimisation is directly visible, the fundamental thrust is increased by 4.26% compared to that obtained with the PSO dimensions. The ripple force is reduced by 99.968% compared to that obtained with the PSO dimensions.



(a) Total Thrust



(b) Force Ripple

Figure 4.8: Thrust variation generated by a TPMA with VEPSO dimensions

Chapter 5

Improvement and further research

The objective of this chapter is to present several improvements that can be made to the analytical model. The improvements to be made to the analytical model serve essentially to refine the results obtained so that they are as close as possible to the results that would be obtained experimentally. These improvements then aim to minimise the number of assumptions that have been made about the analytical model.

An introduction to the use of TPMA as an active suspension is then developed. It serves essentially to introduce a dynamic use of TPMA for future research on this subject.

5.1 Finite permeability back iron parts

The first assumption made in Chapter 2 was to consider that the back iron parts have infinite permeability, thus simplifying the analytical model by reducing the number of boundary conditions. If the model is to be more complete, it is imperative to consider that the back iron parts have a finite permeability and therefore to consider them as a sub-domain of the TPMA.

A new boundary condition between PMs and back iron shares should therefore be imposed. Since the back iron parts have a finite permeability, it is now possible to apply the continuity condition between the radial component of the magnetic flux density of PMs and back iron parts. A Dirichlet boundary condition must be imposed at the inner edge of the internal back irons part and at the outer edge of the external back iron part. This boundary condition is illustrated in Figure 5.1. This results in the following equation to be imposed

$$A_\phi|_{r=R} = 0 \quad (5.1)$$

where R is the radius of the inner edge of the internal back iron part or the radius of the outer edge of the external back iron part.

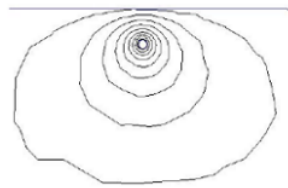


Figure 5.1: Dirichlet boundary condition [30]

Imposing these boundary conditions implies that the back iron parts have an expression for the

radial and axial magnetic flux density. Thus a certain level of magnetic flux density in these regions can be observed. Thus knowing the material used for the back iron parts, it is possible to compare the magnetic flux density levels with the B-H curve and check where these levels are situated with respect to this curve. Thus the analytical model still does not allow for saturation within the back iron parts, but it does allow us to know if saturation is present with the current design. If saturation is observed, it can be reduced by changing the thickness of the back iron parts or the PMs [3].

5.2 Finite length TPMA

One of the assumptions made before developing the analytical model is to consider that the TPMA is of infinite length in order to neglect the edge effects. This assumption simplifies the analytical model the most and has the greatest impact on the results obtained.

Considering that the TPMA is of finite length implies directly that there will be the presence of edge effects at the axial edges. Thus the PMs present at the axial edges of the TPMA produce a flow that is not completely linked to the following PM. Thus part of their magnetic flux takes a path through the air and back into the back iron parts, they are called fringing flux. Another part of these fluxes leaks directly out of the TPMA [31]. These effects, called longitudinal end effects, are illustrated in Figure 5.2.

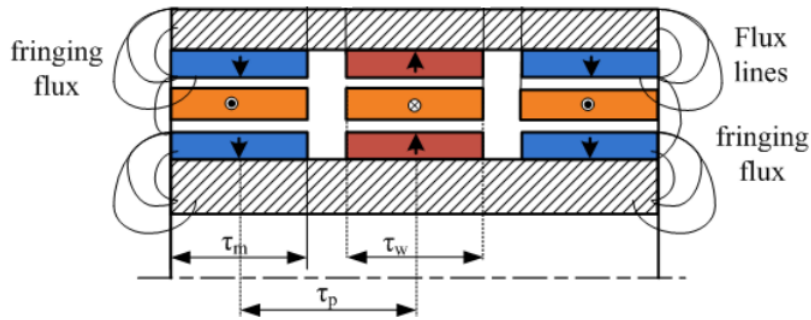


Figure 5.2: Illustration of end effects for a finite length TPMA [3]

The magnetic flux density for a TPMA of finite length can be determined using the subdomain method with Fourier expansion which is the method employed in Chapter 2. However, many boundary conditions at the axial edges must be introduced. These boundary conditions are asymptotic. That is, they are a combination of Dirichlet boundary conditions and Neumann boundary conditions. Implementing these boundary conditions will result in poor conditioning of the coefficient determination matrix. In case the coefficients are correctly calculated, the analytical method would lose all its advantage over the Finite Element Method (FEM) as the calculations would be excessively long [3].

Another method, presented in [32], is to place an infinite series of TPMA's at a certain distance from each other. However, this method always assumes that the back iron has infinite permeability, which means that the asymptotic boundary conditions must always be introduced, whereas the magnetisation vector is easily calculated using the Fourier expansion. Thus an alternative method is presented in [3] where the back iron is infinitely long but has finite permeability. The PMs are considered as an infinite series of discrete arrays. This alternative method is illustrated in Figure 5.3 for a TPMA with radially magnetized PMs. Thus this alternative method allows to develop for a TPMA of finite length the analytical model which approximates the magnetic flux density distribution. The mathematical

development is similar to that developed in Chapter 2 except that it is based on the diagram in Figure 5.2.

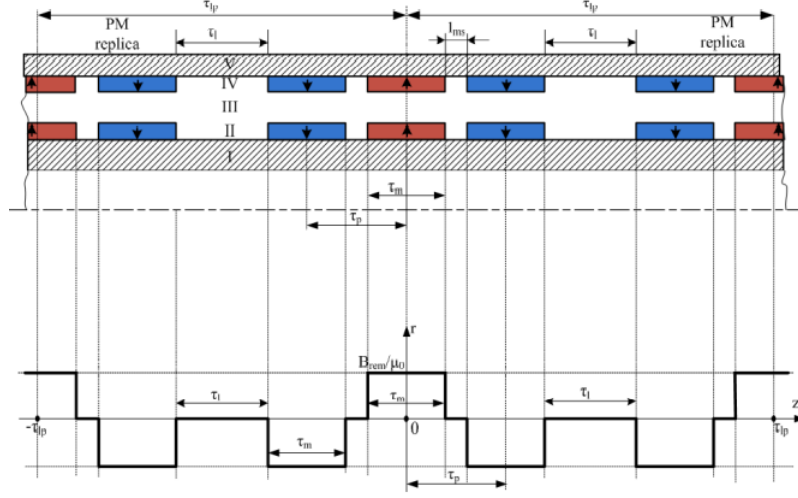


Figure 5.3: Structure of the TPMA with infinitely long back iron and with series PM-array

5.3 Armature field reaction

When the coils in the armature have current flowing through them, they produce a magnetic field. This phenomenon is called the armature reaction field and can distort the magnetic field produced by the PMs.

This phenomenon has been neglected in this thesis because it has minimal influence on the main magnetic field when an air-cored armature is studied and when the TPMA is under magnetostatic conditions. However, when it comes to establishing control design schemes on the TPMA, the armature reaction field has a significant impact on the thrust produced. This is mainly due to the high variation in current flowing through the coils during the dynamic phases of TPMA operation.

In [33], the method of solving for the expression of the armature field reaction is essentially the same as that used in Chapter 2. Maxwell's equations are again solved using the technique of variable separation with Fourier series. The point that changes with respect to the solution developed in Chapter 2 is the right-hand side of the Poisson equation. Indeed, in the case of the armature region, unlike the PM region, the magnetisation vector is zero but the current density vector is not. Thus the equation in the armature region takes the form

$$\nabla^2 \mathbf{A} = -\mu \mathbf{J} \quad (5.2)$$

The calculation of the field reaction reinforcement can therefore be of interest when studying the dynamic behaviour of the TPMA because in this case it has a non-negligible impact on the thrust produced.

5.4 Incorporation of TPMA into the suspension system

This section serves as a basis for considering the incorporation of the TPMA design developed in this work into an active suspension system. The suspension system chosen is that of a train's car as the TPMA has been designed in this way.

The diagram of the suspension system is shown in Figure 5.4 and it can be seen that the primary suspension is a passive suspension (a spring in parallel with a damper) and the secondary suspension is an active suspension represented by the TPMA in parallel with a passive suspension. The purpose of the primary suspension is to reduce the vibrations caused by the road between the wheel and the bogie. The purpose of the secondary suspension is to isolate the body vehicle from the bogie as much as possible. Its objective is to improve passenger comfort as much as possible.

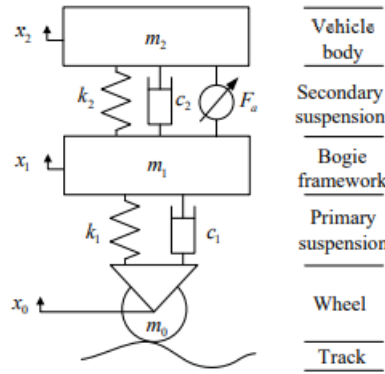


Figure 5.4: Active suspension model of 1/4 train's car [34]

The system shown in Figure is the simplified 2-Degrees Of Freedom (DOF) model, the full model being 7-DOF. However, it allows the system behaviour to be well represented with fewer parameters [34]. The equations of motion are obtained by applying Newton's second law

$$m_1 \ddot{x}_1 = -k_2 (x_1 - x_2) - c_2 (\dot{x}_1 - \dot{x}_2) + k_1 (x_0 - x_1) + c_1 (\dot{x}_0 - \dot{x}_1) - F_a \quad (5.3)$$

$$m_2 \ddot{x}_2 = k_2 (x_1 - x_2) + c_2 (\dot{x}_1 - \dot{x}_2) + F_a \quad (5.4)$$

where m_1 and m_2 are mass of the bogie and the vehicle body respectively, x_1 and x_2 are the vertical displacement of the bogie and the vehicle body respectively, k_1 and k_2 are the elastic stiffness of the primary and secondary suspension respectively, c_1 and c_2 are the damping coefficient of the primary and secondary suspension respectively, x_0 is the excitation that corresponds to the irregularities of the road and F_a is the active control force generated by the TPMA.

The only active parameter is F_a and can therefore be controlled to minimise vehicle vibration. Thus the principle of inverse actuator dynamics is applied. A certain dynamic, that of vibration, will be imposed on the TPMA. Thus a certain control force F_a must be produced in order to reduce the vibrations. This force is calculated using Equations 5.3 and 5.4 and also using control parameters.

Since the control force is known by the dynamics imposed on it, it remains to determine the current to be injected into the windings of the TPMA. Two current variables are therefore to be controlled: the current density and the current frequency. Firstly, the current density is linearly related to the control force. This relationship, for a TPMA with the optimised dimensions of the Table 4.2, is illustrated in Figure 5.5. Note that the force is expressed in terms of pole pitch.

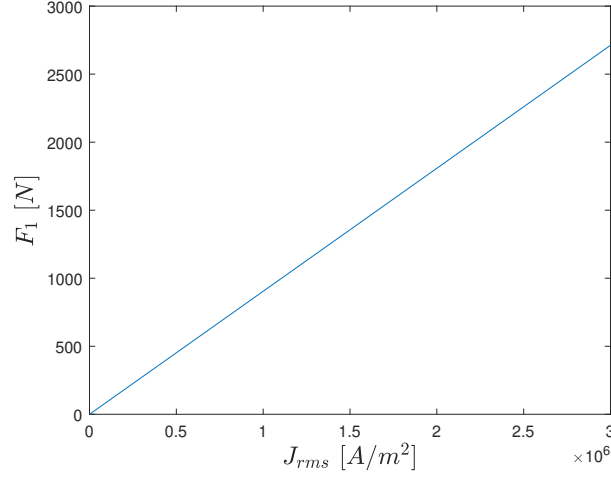


Figure 5.5: Fundamental force as a function of current density

Then the current frequency is obtained directly from the synchronous relationship between the armature and the PM

$$\omega = \frac{\pi v}{\tau_p} \quad (5.5)$$

thus the frequency is directly obtained by the dynamics imposed on the TPMA with v being the relative speed of the armature with respect to the PMs. The speed of the armature is directly related to the variation in the travel of the secondary suspension which is given by $\dot{x}_2 - \dot{x}_1$.

It is then necessary to describe the control process of the TPMA within the active suspension. The block diagram of the active suspension is shown in Figure 5.6. It can be seen that the controller is at

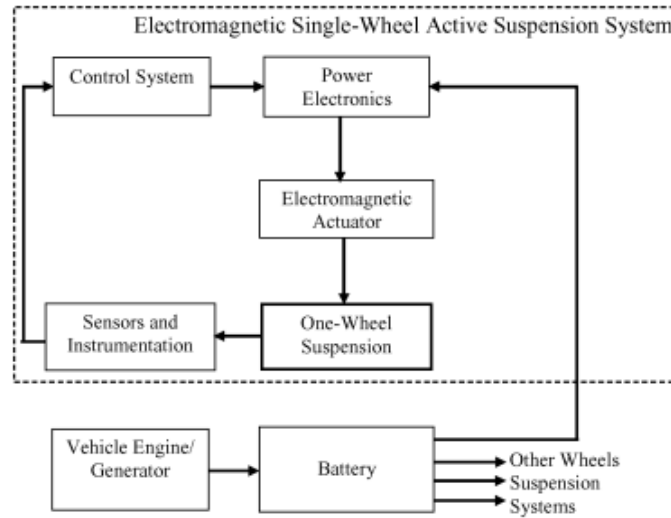


Figure 5.6: Block diagram of an electromagnetic active suspension [35]

the centre of the system as it receives the vehicle status information collected by the sensors. It then generates the appropriate power control signals. These control signals then supply the TPMA with a current of the desired magnitude and frequency.

The objectives of future research on this topic would be

- Select a control algorithm for the TPMA. This algorithm will need to take the correct inputs and outputs in order to deliver the correct control current to the TPMA.
- The analytical model describing the active suspension system can be developed to see how well the TPMA and the control system work when the suspension system experiences a signal that corresponds to road irregularities.

Chapter 6

Conclusion

This master thesis presented an optimised TPMA design capable of being implemented in an active railway suspension system.

In the first part of this thesis, a description of the operating principle of the TPMA has been made. Then a state of the art of the possible topologies of TPMA were presented. Their complete structure has also been presented.

In the second part of the thesis, the analytical model of each of the topologies presented in the first part has been developed. Before establishing the governing equations common to each of the topologies, the assumptions made on each model are established. Then the Laplace and Poisson equations are solved according to the specificity of each topology. In order to obtain the solutions for the magnetic flux densities, the boundary conditions specific to each topology are established. Finally, the results are plotted and compared. It is found that the dual Halbach array topology obtains the highest radial component of the magnetic flux density in the air gap region with a peak at over 0.3 [T]. This topology has therefore been retained for the rest of the thesis.

In the third part of the thesis, an analytical model of the thrust produced by the TPMA was developed. This model is based on the use of Laplace's equation which relates the magnetic flux density produced by the PMs and the current flowing through the armature windings. A comparison between the different types of current to be injected, single-phase, double-phase and three-phase, was carried out to see which produced the most thrust and the least ripple force. The current that provides the best compromise is three-phase, which produces less maximum thrust than single-phase, 1152.31 [N] versus 1502.61 [N], but produces significantly less ripple force since the thrust produced using single-phase current varies between 0 and maximum thrust. Thus the use of three-phase current is retained in the rest of the thesis.

The fourth part of the thesis is focused on an optimisation of the geometrical dimensions of the TPMA. In the first instance, the optimisation focuses only on the maximisation of thrust. Five dimensions are to be optimised: R_1 , R_2 , R_3 , R_4 and τ_p . The optimisation of these dimensions was obtained using the PSO method. After this first optimisation, the TPMA with the optimised dimensions grouped in Table 4.1, produces a fundamental thrust of 1341.47 [N] which is 21.29 % higher for the same volume than that produced with the standard dimensions used in the previous chapters.

Then a second optimisation was performed using a method derived from PSO for multi-objective optimisation, the VEPSO. Indeed, in addition to maximising thrust, the second objective was to

minimise the ripple force. Only three parameters were to be optimised: R_2 , R_3 and α . After this further optimisation, the R_2 with the optimised dimensions grouped at Table 4.2, produces a 4.26 % higher thrust than that produced after the first optimisation as well as a 99.968 % reduction in ripple force. It was stated that such a low ripple force was not achievable in reality because the edge effect was not taken into account and such precise dimensions were hardly achievable. However, it can be seen that the optimisation algorithm really performs well even if the results still need to be interpreted.

In the fifth and last part of the thesis, several improvements that can be made to the analytical model such as considering the TPMA of finite length, considering the armature field reaction or considering that the back iron parts have a finite permeability have been presented. Then an introduction on the incorporation of TPMA in an active train suspension system was presented.

Bibliography

- [1] écoconso. URL: <https://www.ecoconso.be/fr>.
- [2] Liang Yan, Lu Zhang, Juanjuan Peng, Lei Zhang, and Zongxia Jiao. *Electromagnetic Linear Machines with Dual Halbach Array*. Springer Science, 2017. ISBN: 978-981-10-2307-1.
- [3] Dickson Kanungwe Chembe. *An Analytical Model of a Radially Magnetised Longitudinal-Flux Permanent Magnet Air-cored Linear Oscillatory Machine*. PhD thesis, University, Stellenbosch, South Africa. December 2019.
- [4] Jun-Ho Yoon, Dongwook Kim, No-Cheol Park, and Young-Pil Park. “Design of a Tubular Permanent Magnet Actuator for Active Lateral Secondary Suspension of a Railway Vehicle”. In: *MDPI Applied sciences* vol. 7, February 2017.
- [5] Jiabin Wang. “A general framework for the analysis and design of tubular linear permanent magnet machines”. In: *IEEE Transactions on Magnetics* vol. 35.no. 3, June 1999.
- [6] Ashabani M., Mohamed Yasser, and Milimonfared Jafar. “Optimum Design of Tubular Permanent-Magnet Motors for Thrust Characteristics Improvement by Combined Taguchi–Neural Network Approach”. In: *Magnetics, IEEE Transactions on* 46, January 2011.
- [7] Christof Rohrig and Andreas Jochheim. “Identification and compensation of force ripple in linear permanent magnet motors”. In: *Conference Paper in Proceedings of the American Control Conference*, February 2001.
- [8] Yan Liang, Zhang Lei, Yao Jianyong, Hu Hongjie, Chen Chin, and Chen I-Ming. “A tubular linear machine with dual Halbach array”. In: *Engineering Computations* 31, April 2014.
- [9] Wang Jiabin and Howe D. “Tubular modular permanent-magnet machines equipped with quasi-Halbach magnetized magnets - Part I: Magnetic field distribution, EMF, and thrust force”. In: *Magnetics, IEEE Transactions on* vol. 41, October 2005.
- [10] HSMAG. *What is a Halbach Array?* URL: <https://www.hsmagnets.com/blog/halbach-array>.
- [11] Wikiwand. *Halbach array*. URL: https://www.wikiwand.com/en/Halbach_array.
- [12] Arthur Matyas and Daniel Fodorean. “Multi-phase synchronous motor solution for steering applications”. In: *Progress In Electromagnetics Research* vol. 131, January 2012, pp. 63–80.
- [13] Koen J Meessen, Koen J Meessen, and E.A. Lomonova. “Analysis and design of a slotless tubular permanent magnet actuator for high acceleration applications”. In: *Journal of Applied Physics* vol. 105, May 2009.
- [14] Benoît Vanderheyden. “Chapître 3 : Magnétostatique”. In: *ELEN0076-1 Electromagnétisme*, 2021-2022.
- [15] Liang Yan Nan Yao, Tianyi Wang, and Shaoping Wang. “Magnetic Flux Distribution of Linear Machines with Novel Three-Dimensional Hybrid Magnet Arrays”. In: *MDPI Sensors* vol. 17, November 2017.

- [16] A. Baricz and T. K. Pogany. “Integral Representations And Summations Of The Modified Struve Function”. In: *Acta Mathematica Hungarica* vol. 141, November 2012.
- [17] Liang Yan, Lu Zhang, Lei Peng, and Zongxia Jiao. “Comparative Study of the Dual Layer Magnet Array in a Moving-Coil Tubular Linear PM Motor”. In: *MDPI Sensors* vol. 18.no. 3, June 2018.
- [18] Matthew N. O.Sadiku. *Elements of Electromagnetics*. Seventh Edition. The Oxford Series In Electrical And Computer Engineering. Oxford University Press, 2018. ISBN: 9780190698614.
- [19] Pablo Martin, Eduardo Rojas, Jorge Olivares, and Adrián Sotomayor. “Quasi-Rational Analytic Approximation for the Modified Bessel Function with High Accuracy”. In: *MDPI Symmetry* vol. 13, April 2021.
- [20] Gysen B.L.J., Meessen K.J., Paulides J.J.H., and Lomonova E.A. “General Formulation of the Electromagnetic Field Distribution in Machines”. In: *IEEE Trans. Magn* vol. 46, January 2010.
- [21] Liang Yan, I-Ming Chen, Chee Kian Lim, and Guilin Yang. *Design, Modeling and Experiments of 3-DOF Electromagnetic Spherical Actuators*. Springer Dordrecht. MECHANISMS AND MACHINE SCIENCE Volume 4. 2011.
- [22] Liang Yan, Lei Zhang, Nan Yao, Tianyi Wang, Zongxia J, and I-Ming Chen. “Force Formulation of a Three-phase Tubular Linear Machine with Dual Halbach Array”. In: *IEEE 10th International Conference on Industrial Informatics*, 2012.
- [23] S.N Sivanandam and S.N Deepa. *Introduction to Genetic Algorithms*. Springer Berlin, Heidelberg. 2008.
- [24] Faisal Alqahtani, Ema Michael Abraham, Essam Aboud, and Murad Rajab. “Two-Dimensional Gravity Inversion of Basement Relief for Geothermal Energy Potentials at the Harrat Rahat Volcanic Field, Saudi Arabia, Using Particle Swarm Optimization”. In: *MDPI Energies* vol. 15, April 2022.
- [25] Perez R.E and Behdinan K. “Particle swarm approach for structural design optimization”. In: *Computers structures* vol. 85, 2007.
- [26] Maurice Clerc and James Kennedy. “The Particle Swarm—Explosion, Stability, and Convergence in a Multidimensional Complex Space”. In: *IEEE Transactions on Evolutionary Computation* vol. 6, February 2002.
- [27] Shi Yao Lim, Mohammad Montakhab, and Hassan Nouri. “A Constriction Factor Based Particle Swarm Optimization For Economic Dispatch”. In: *The 2009 European Simulation and Modelling Conference*, October 2009.
- [28] Omkar S.N, Mudigere Dheevatsa, Naik G. Narayana, and Gopalakrishnan S. “Vector evaluated particle swarm optimization (VEPSO) for multi-objective design optimization of composite structures”. In: *Computers structures* vol. 86, 2008.
- [29] K.Deb. *Multi-Objective Optimization using Evolutionary Algorithms*. John Wiley and Sons. 2001.
- [30] R Bargallo. *Finite Elements for Electrical Engineering*. Polytechnic University of Catalonia. 2006.
- [31] Wang J., Howe D., and Jewell G.W. “Fringing in Tubular Permanent-Magnet Machines: Part II. Cogging force and its minimization”. In: *IEEE Trans. Magn* vol. 39, 2003.
- [32] Chen X., Zhu Z., and D. Howe. “Modeling and Analysis of a Tubular Oscillating Permanent-Magnet Actuator.” In: *IEEE Trans. Ind. Appl.* vol. 45, 2009.
- [33] Yan L., Zhang L., Jiao Z., Hu H., Chen C.Y., and Chen. “I.M.: Armature reaction field and inductance of coreless moving-coil tubular linear machine”. In: *IEEE Trans. Ind. Electron* vol. 62, 2014.

- [34] Shichang Dong, Jianjun Meng, Decang Li, and Hao Song. “Performance Analysis of Giant Magnetostrictive Actuator and Its Application on Active Suspension of Train”. In: *Latin American Journal of Solids and Structures* vol. 18, August 2021.
- [35] Ismenio Martins, Jorge Esteves, Gil D. Marques, and Fernando Pina da Silva. “Permanent-Magnets Linear Actuators Applicability in Automobile Active Suspensions”. In: *IEEE Transactions On Vehicular Technology* vol. 55, January 2006.